Characterization of cortical neurodevelopment *in vitro* using gene expression and morphology profiles from single cells

Adithi Sundaresh[1,*], Dimitri Meistermann[1,*], Riina Lampela[1], Zhiyu Yang[2], Rosa Woldegebriel[1], Andrea Ganna[1,2,3], Pau Puigdevall[1], Helena Kilpinen[1,2,4,#]

1. Helsinki Institute of Life Science (HiLIFE), University of Helsinki, Finland
2. Institute for Molecular Medicine Finland (FIMM), University of Helsinki, Finland
3. Faculty of Medicine, University of Helsinki, Finland
4. Faculty of Biological and Environmental Sciences, University of Helsinki, Finland
** Equal contribution*
# Corresponding author

Abstract

Differentiation of induced pluripotent stem cells (iPSC) towards different neuronal lineages has enabled diverse cellular models of human neurodevelopment and related disorders. However, *in vitro* differentiation is a variable process that frequently leads to heterogeneous cell populations that may confound disease-relevant phenotypes. To characterize the baseline and diversity of cortical neurodevelopment *in vitro*, we differentiated iPSC lines from multiple healthy donors to cortical neurons and profiled the transcriptomes of 60,000 single cells across three timepoints spanning 70 days. We compared the cell types observed *in vitro* to those seen *in vivo* and in organoid cultures to assess how well iPSC-derived cells recapitulate neurodevelopment *in vivo*. We found that over 60% of the cells resembled those seen in the fetal brain with high confidence, while 28% represented metabolically abnormal cell states and broader neuronal classes observed in organoids. Further, we used high-content imaging to quantify morphological phenotypes of the differentiating neurons across the same time points using Cell Painting. By modeling the relationship between image-based features and gene expression, we compared cell type- and donor-specific effects across the two modalities at single cell resolution. We found that while morphological features capture broader neuronal classes than scRNA-seq, they enhance our ability to quantify the biological processes that drive neuronal differentiation over time, such as mitochondrial function and cell cycle. Finally, we show that iPSC-derived cortical neurons are a relevant model for a range of brain-related complex traits. Taken together, we provide a comprehensive molecular atlas of human cortical neuron development *in vitro* that introduces a relevant framework for disease modeling.

Keywords: stem cells, iPSC, differentiation, neurodevelopment, cortical neurons, single-cell genomics, transcriptomics, cell painting, high-content imaging, disease modeling

Introduction

Induced pluripotent stem cells (iPSCs) are a powerful tool to model human diseases and traits. In particular, iPSC-derived neurons and glia have revolutionized the study of brain-related disorders, which previously relied heavily on animal models and post-mortem tissue. However, iPSC-based differentiation systems are inherently variable[1–3] and for any given protocol, the full spectrum of cell types generated *in vitro* is often not known. For example, *in vitro* conditions can give rise to cell types and states that are not seen *in vivo*[4]. To this end, single-cell RNA-sequencing (scRNA-seq) technology has transformed the resolution at which iPSC-derived cell types can be characterized. A recent study integrated over 1.7 million cells from human neural organoids and characterized the cell types and states generated by 26 different protocols[5]. They found that a fraction of the *in vitro* neurons presented metabolic states that differed from their *in vivo* counterparts, linked to cell stress induced by the *in vitro* conditions. Further, while informative, gene expression levels alone do not comprehensively capture cellular function and the biological processes that ultimately drive disease pathophysiology in tissues, organs, and whole organisms, highlighting the need for complementary cellular readouts.

In this study, we used scRNA-seq to characterize cell type heterogeneity in an established 2D cortical neuron differentiation system based on dual-SMAD inhibition, chosen for its reported ability to recapitulate the progression of neurodevelopment *in vitro*[6,7]. We collected transcriptomic data from >60,000 cells from four healthy donors across three time points corresponding to early progenitors (day 20), intermediate progenitors (day 40) and maturing cortical neurons (day 70) (**Fig. 1a**) and compared them to fetal cell types *in vivo* (**Fig. 1b**). To systematically explore cellular phenotypes beyond the transcriptome, we also assayed the differentiating neurons with Cell Painting (CP), a high-content, multiplexed image-based method to capture cellular morphology[8,9] (**Fig. 1c**). Cell Painting uses fluorescent dyes to label different basic organelles of the cell, such as the nucleus, mitochondria, and the endoplasmic reticulum (ER) from which hundreds of image-based features can be derived, representing the morphological profile of each cell. In order to link transcriptomic features to cell-level morphological phenotypes, we analyzed the CP data at a single-cell resolution and, by leveraging a predictive model[10], provide links between image features and gene expression levels in developing cortical neurons (**Fig. 1d**).

We observed that even for a small number of iPSC lines, links between gene expression and morphological features recapitulate known cell biology, as previously reported[11]. We also found that donor-specific changes were recapitulated by both assays, and image-based features can offer insights on the dynamics of morphological readouts, as observed with changes in mitochondrial intensity over time. However, our results suggest that characterization of a heterogeneous system based on cellular morphology requires targeted development of the CP assay for the cell types of interest[12], as well as larger sample sizes to generalize the results. Taken together, we present here a single-cell atlas of 2D cortical development that draws from both transcriptomics and cellular morphology measurements to establish a phenotypic baseline for subsequent disease modeling studies.

Results

1. Characterizing cell type diversity of cortical neuron development *in vitro*

We differentiated iPSCs from four donors towards cortical neuronal fate and characterized them at days 20, 40 and 70 of the differentiation using scRNA-seq and Cell Painting (**Tables 1, S1-S4**). As a preliminary benchmarking of whether the three timepoints captured the expected cell types, we confirmed expression of canonical markers of neural progenitors (*NESTIN*), intermediate progenitors (*EOMES*) and neurons (*TUJ1*) via immunocytochemistry[6] (**Fig. 1d, S1a**) (**Tables S5-6, Methods**). We then leveraged scRNA-seq data to further classify the cell types of the 60,000 cells present in our dataset. It has been established previously that *in vitro* generated neurons more closely resemble fetal rather than adult neuronal cell types[13,14]. We thus used the reference mapping approach (**Methods**) from the Seurat package[15] to transfer cell type labels from a well-annotated mid-gestation (gestational weeks 17-18) fetal reference[16] onto our query dataset. With this approach, we annotated cells without being limited to a few canonical markers, aiming to better describe the dynamics of *in vitro* cortical differentiation. We identified 15 cell types produced across the three time points, capturing a large portion of the heterogeneity seen in developing neurons (**Fig. 1b**). These include various progenitor cell types (cycling progenitors, ventral and outer radial glia) as well as intermediate progenitors and maturing neuronal cells (deep layer and maturing upper layer excitatory neurons). As has been reported recently[17], we also note the production of inhibitory neurons within our cortical system (MGE- and CGE-like interneurons).

To further probe the extent to which *in vitro* differentiated cells resembled those produced *in vivo*, we correlated the expression profiles of query and reference cell types (**Methods**). Although our annotated cell types showed the highest correlation to the equivalent fetal cell types (mean R=0.50, off-diagonal mean R=0.05) (**Fig. S1b**), the specificity of the *in vitro* cell types to the fetal cell types improved (mean R=0.55, off-diagonal mean R=0.03) (**Fig. S1c**) after retaining only high-confidence predictions[18] (mapping scores >0.5). Approximately 40% of the cells fell below this threshold and remained unmapped. Further, the proportions of the annotated cell types varied as expected across time points, with progenitors being more abundant at the earliest stage and decreasing at day 40 and 70, whereas neuronal cells followed the opposite trend (**Fig. 1f**). We additionally detected donor-to-donor variation as is expected from iPSC-based models[1,2], with two specific cell types showing differential abundance - pericytes and inhibitory neurons (**Fig. 1f**).

2. Cell Painting for phenotyping developing neurons at the single-cell level

Cellular organelles such as mitochondria and the ER are known to play an important role in neurodevelopment, specifically in meeting dynamic energetic and metabolic requirements[19]. Aiming to characterize the morphological features of developing neurons *in vitro*, we assayed six cell lines (n=4 donors) with Cell Painting at days 20, 40 and 70 of the differentiation, originating from the same samples used in day 20 of scRNA-seq (**Methods**). Image-based features such as fluorescence intensities, texture and cell shape measures obtained from each CP channel represent the overall morphological profile of the cell. These features were extracted into a matrix per single cell, and, after quality control and regularization (**Methods**), we obtained a feature matrix of 223 features from 54,415 cells. Well-to-well correlation indicated that differentiation day was, as expected, the major source of variation (**Fig. S2a**). The feature matrix was then analyzed in a similar manner to scRNA-seq data. Thus, Leiden clusters projected on a Uniform Manifold Approximation and Projection (UMAP) (**Fig. 2a**) describe the main phenotypic states captured by Cell Painting.

In light of the high modularity of CP features, we defined feature modules based on the correlation between CP features (**Figs. 2b**, **S2b**). Correlated features within the same module usually corresponded to multiple aspects of the same measurement, for example cell area and perimeter, or the average and minimum intensity of each channel. Interestingly, there was a global correlation between the channel comprising the cell membrane, Golgi apparatus, actin cytoskeleton and nucleoli (CGAN) and the ER channel. In contrast, some pairs of Cell Painting features were highly anticorrelated (**Fig. S2b**). In our study, this was observed between cell size and density, suggesting that smaller cells are more likely to be found in areas of higher density (**Fig. S2c**). Furthermore, a near-perfect negative correlation was detected between 'Angular Second Moment' texture values and the intensity within each channel. This phenomenon suggests that these two measurements may represent inverse aspects of the same underlying characteristic.

The distribution of feature values shows that despite the difference between timepoints, CP was able to capture a relative continuity across them. Clusters composed mainly of day 20 cells were characterized by high intensities for the mitochondria channel (**Fig. 2b-c**), and clusters with mainly day 40 cells by medium mitochondria intensity and high ER intensity. Interestingly, day 70 was the most heterogeneous timepoint with three distinct profiles: cells with a large area that were close to d40 cells in terms of features value ('d70.bigCells'), cells with very low mitochondria intensity ('d70.mitoNeg') and cells that clustered with d20 cells ('d70_20.mito').

To improve the interpretability of CP features and link them to gene expression, we modeled the relationship between Cell Painting and scRNA-seq. Similarly to Haghighi *et al.*[10], we used the common experimental design between the two assays to train lasso regression models that can be used to predict the corresponding CP feature values of the scRNA-seq dataset (**Methods**). We then used the model coefficients matrix to perform a functional enrichment, using the median of gene coefficients per feature module as an input to Gene Set Enrichment Analysis (GSEA) (**Fig. 2b**, **Supplementary Data 1**)[20,21]. The analysis revealed a significant redundancy among the enriched terms observed, with a predominant focus on the proteasome, extracellular matrix, and mitochondrial respiration. This pattern underscores the tendency of Cell Painting to predominantly capture variation related to cell morphology rather than specific pathway regulation. In most cases, the enriched terms per module were closely linked to the module-associated features, increasing the confidence in our model. The enrichment of terms related to the ER membrane in a module composed of features associated with the ER channel is a notable example. Interestingly, other general terms such as intensity of mitochondria were more linked to mitochondrial ribosomes than mitochondrial respiration or oxidative phosphorylation. A small pool of d20 cells ('d20.nucNeg') was particularly linked with mitosis. To further explore the possible link between CP and cell cycle, we predicted the cell cycle scores (G2M score, S score) in the CP dataset by using the predicted CP features matrix on scRNA-seq profiled cells and their annotated cell cycle scores (**Methods**). Using our regression model, 'd20.nucNeg' cells showed the highest median values for both G2M score and S score, and, coupled with their particular morphology (**Fig. 2d**), suggests that CP is able to capture cycling cells at least at day 20.

We also used the predicted CP feature matrix to assess the correlation between CP clusters and the cell types inferred from scRNA-seq (**Fig. 2e**). The low specificity of this correlation did not enable distinguishing individual cell types, as multiple cell types exhibited correlation with CP clusters. Conversely, multiple CP clusters correlated with a single cell type. Rather, a general pattern emerged distinguishing "neuronal" cell types from other cell types based on the relationship between specific groups of cell types and CP clusters. This pattern demonstrates the efficacy of Cell Painting in classifying these two broad categories of cells, yet it also highlights its limitations in differentiating between subclasses of neurons.

3. Neurodevelopment *in vitro* follows known trajectories and recapitulates cell type heterogeneity seen *in vivo*

Neurodevelopment *in vivo* is characterized by a tightly regulated developmental trajectory, from neural progenitors to radial glia and, via intermediate progenitors, to maturing neurons. By constructing the pseudotime trajectory of our differentiating cells across the three time points (**Methods**), we found that the developing cells *in vitro* follow a similar trajectory as seen *in vivo* (**Fig. 3a**). Additionally, by computing gene modules changing as a function of pseudotime with the Monocle3 toolkit, we identified gene sets linked to the development of individual cell types (**Fig. S3a**). These gene sets were enriched for many expected biological processes, such as ‘nuclear division’ in PgG2M cells and ‘ribonucleoprotein complex biogenesis’ in PgS (**Fig. S3b-f**). The IP-associated module was tagged by terms such as ‘cell fate commitment’ and ‘channel activity’, indicative of the transitory role these cells play between progenitors and neurons. Neuronal modules were characterized by formation and regulation of synapses as well as ion channel activity, with the inhibitory neuron-associated module linked to GABA signaling.

From the CP data we observed a distinct pattern of mitochondrial features across the UMAP, with mitochondrial intensity-related features more prominently associated with d20 cells and decreasing towards d70, whereas mitochondrial texture-associated features (angular second moment) followed the opposing trend (**Fig. 3b**). To associate this trend with specific cell types, we projected these CP features onto the scRNA-seq UMAP confirming that the trend is maintained; mitochondrial intensity is higher amongst progenitor cell types, whereas angular second moment is higher amongst mature/maturing neurons, representing uniform texture (**Fig. 3c**). The notable exception is the region of the UMAP occupied by inhibitory neurons, specifically MGE-like interneurons, which instead have high mitochondrial intensity and low angular second moment.

Given the cell-type specificity of mitochondrial CP features, we sought to determine whether we could detect changes in the transcription profile linked to mitochondrial metabolism. It has been reported previously that NPCs meet their energetic requirements primarily through glycolytic pathways, and the switch to neuronal fate is associated with a switch to dependency on oxidative phosphorylation (‘OxPhos’)[22]. Gene set variation analysis (GSVA) on pseudo-bulked cell types for both glycolysis and OxPhos (**Methods**) confirmed that most neuronal cell types had lower glycolytic dependency, with all excitatory cell types showing maximum activation for OxPhos except for ExDp1 (**Fig. 3d**). We further tested for enrichment of gene ontology (GO) terms associated with mitochondria in the gene expression patterns per cell type, finding a clear link between the progenitor cell types and mitochondrial ribosomal subunits, whereas mature cell types were linked to mitochondrial membrane components, known to be linked to OxPhos (**Fig. 3e**). These findings complement the trend observed from the functional enrichment of CP feature modules, where day 20 clusters were enriched in mitochondrial ribosome and mitosis, day 40 in transcriptional regulation, and day 70 in oxidative phosphorylation (**Fig. 2b**).

4. Metabolic differences shape high versus low quality cells produced *in vitro*

Although our *in vitro* differentiated cells recapitulated *in vivo* processes, the 'unmapped' cells still represented a non-negligible fraction (~40%) whose identity remained unexplained. Further, the unmapped cells were found to be present across the UMAP (**Fig. 4a**), likely indicating that cells did not fully resemble the fetal transcriptomes and/or were transitioning between cell types, rather than being a single missing or unannotated cell type. By assigning the highest scoring cell type label to each cell in the unmapped fraction of cells, we divided our dataset into high and low quality (HQ/LQ) cells for each annotated cell type (**Methods**). The LQ cells still expressed canonical markers of the cell type they were closest to, although at lower levels, except in the case of oRG and IPs (**Fig. S4a**). Additionally, LQ cells did not show consistent differences in pseudotime scores as compared to HQ cells of the same cell type (**Fig. S4b**), which would have been indicative of transitioning cell states. Given this, we assessed what transcriptomic features were driving their lower mapping scores. By comparing differential activation of developmentally relevant pathways between high- and low-quality cells per cell type, we identified those that differed (**Fig. 4b**). Importantly, although metabolic processes seemed to be implicated overall, we did not see consistent changes across all cell types, rather observing specific changes driving the LQ version of each cell type, such as DNA replication and glycolysis in progenitor cell types (vRG, oRG, IP). Also, we observed the highest steroid biosynthesis activation in mapped maturing excitatory neurons (ExM) compared to unmapped, but the opposite trend was observed within progenitors (PgS, PgG2M).

Aberrant cellular metabolism has previously been reported in other *in vitro* systems, often highlighted in the oxidative phosphorylation and glycolytic pathways[5,23]. In cortical organoids, it has been seen that a fraction of cells does not recapitulate distinct fetal cellular identities[4]. Hypothesizing that our unmapped cells represented a similar fraction, we annotated our unmapped cells to cortical organoid cell types from Bhaduri *et al.* (2020)[4] using the same label-transfer method and threshold described above (**Methods**). Upon this, we found that more than 50% of the previously unmapped cells could be attributed to 'pan-radial glial' or 'pan-neuronal' cell types across all three timepoints (**Fig. 4c**). These were described in the original publication as broad progenitor or neuronal cell classes that did not express features distinctive to any one fetal subtype.

We compared the differentially activated pathways between cells of the closest cell types that passed this bottleneck of subtype acquisition to those that maintained a pan-cell identity. Similar to differences observed between high- and low-quality progenitor cell types, pan-radial glia differed in ribosome-associated pathways. Pan-neuronal cells, however (ExPanNeu-O), were characterized by features of both excitatory and inhibitory neurons, differing again metabolically such as in oxidative phosphorylation or steroid biosynthesis. We identified modules of the top genes driving differentially activated pathways in these cell types and, by scoring these gene modules per single cell (**Methods**), assessed their distribution in multiple neuronal cell types (**Fig. 4d**). We found that overall, pan-neuronal cells appear to be intermediate to either excitatory or inhibitory neuron specification, except for the ribosome pathway.

Additionally, with the inclusion of the second step of annotation, we identified cell types that were initially missed, mainly astrocytes (**Fig. 4c**). While expected to be produced in this protocol, they were absent in our fetal reference, and thus, the first annotation step alone did not identify them. Our experimental workflow involved the use of two versions of the differentiation protocol (original/modified, see **Methods**), differing in enzyme usage for cell dissociation (see **Table S2** for details). To check for potential effects of the protocol on the generation of cell types, we used *miloR*[24] to test for differential abundance of annotated cell types between the protocol versions. At day 40, we found that the astrocyte population (AstroHindb-O) was overrepresented in the modified version of the protocol (**Fig. 4e**).

5. Donor-specific effects drive neuronal cell fate determination

Inhibitory GABAergic interneurons play a key role in cortical circuits by balancing the excitatory/inhibitory activity and by regulating the formation of synapses. Abnormalities in interneuron development, function or migration have been associated with autism spectrum disorder[25,26] and other neurodevelopmental disorders (NDDs)[27,28]. Of the mature neurons identified in our dataset (21%), nearly 40% were annotated as inhibitory interneurons of either caudal or medial ganglionic eminence (InCGE/InMGE).

Although these have canonically been described to originate from brain regions outside of the cortex, *in vitro* studies have previously reported the generation of GABAergic neurons from cortical progenitors[29,30]. A recent study from Delgado *et al.* confirmed via clonal lineage tracing studies that a subpopulation of cortically born GABAergic neurons was transcriptionally similar to ventrally-derived cortical interneurons, but instead arose from cortical progenitors[17]. The InCGE cells from our dataset were characterized by expression of the *DLX* family of genes, as well as *GAD2, DCX* and *MEIS2*. InMGE cells expressed a subset of canonical markers such as *SST, DCX, MEIS2* but, similar to Delgado *et al.*, differed from true ganglionic eminence interneurons in lack of expression of *LHX6* and *NKX2.1* (**Fig. S5a**). This production of interneurons in our system is key to better recapitulate human fetal development considering the relevance of the inhibitory component in neural circuits.

The clustering proximity of these interneurons with excitatory neuronal cell types prompted us to explore the pathways that differed between them. Previous studies both in mice[31] and *in vitro* cultures[30] have indicated the interplay of WNT and SHH signaling as a key player in maintaining the excitatory/inhibitory balance. However, GSVA analysis of KEGG genes associated with these pathways did not show a consistent upregulation of WNT signaling in all excitatory cell types, nor vice versa with Hedgehog signaling for inhibitory cell types (**Fig. S5b-c**). Instead, we found lower values of enrichment scores for oxidative phosphorylation pathway-associated genes in inhibitory than in excitatory neurons (**Fig. 3d,** also seen from GSEA, **Fig. S5d**).

Additionally, as noted earlier, MGE-like interneurons showed marked differences from the other neuronal cell types in CP-based mitochondrial features (**Fig. 3c**). A single donor (HEL61.2) presented an excess of this inhibitory neuronal subtype across time points (**Fig. 5a**). This same donor was overrepresented in the CP cluster 'd20.endoRetNeg', characterized by lowered intensity of the ER channel, and underrepresented in the ER-intense 'd40.endoRet' channel (**Fig. 5b**), pointing towards donor-specific ER effects potentially linked to inhibitory cell fate. Interestingly, we also observed an effect of lowered ribosome-associated genes in gene expression data - the two donors accounting for 80% of inhibitory cell types at days 40 and 70 showed an overall decrease in the KEGG ribosome pathway at these timepoints (**Fig. 5c**). Complementarily, a GSVA of mitochondria-associated GO terms across our *in vitro* cell types (**Fig. 3e**) revealed an overall depletion of mitochondrial ribosome associated genes in inhibitory neurons compared to other cell types, as has been previously reported[32].

In order to elucidate which genes are responsible for the bifurcation between the excitatory and inhibitory fate in our *in vitro* differentiation, we focused on the branch point along the pseudotime trajectory that either produces inhibitory interneurons or IPs, which in turn give rise to excitatory neurons. Within this branch point, we identified modules of genes that were differentially expressed as a function of the pseudotime (**Methods**). As expected, the module marking the inhibitory branch (Module 12, **Fig. S5e**) consisted of TFs known to drive interneuron fate such as the *DLX* family of genes, which was overexpressed in the donor HEL61.2 in d40 progenitors (**Fig. 5d**). In donors producing inhibitory neurons, expression of the *DLX* family increased with pseudotime, peaking at interneuron production. Concordantly, the expression of genes driving the differential activation of the KEGG ribosome pathway (*RPL39* and *RPL19*) also decreased in donors producing inhibitory neurons (**Fig. 5e**). Altogether, our data is indicative of lowered ribosomal activity and mitochondrial differences between excitatory and inhibitory neurons overall.

6. *In vitro* derived cell types capture heritability of brain-related traits

Finally, to evaluate the relevance of our *in vitro* cortical neurons for disease modeling, we used stratified linkage disequilibrium (LD) score regression[33] to quantify how much heritability of common diseases and other traits is enriched within genes that are markers of the cell types generated *in vitro*. We analyzed GWAS summary statistics from a set of 79 common traits including 12 brain-related phenotypes (**Table S7, Fig. S6a-b**) (**Methods**). There was a clear enrichment of significant brain-related associations when accounting for all tests (Fisher Test, $p=9.617 \cdot 10^{-13}$). Comparison of traits captured by *in vitro* cell types (**Fig. 6a**) to those captured by GTEx tissues[34] (**Fig. 6b**) shows that iPSC-derived neurons are relevant for multiple brain-related traits that are associated with the cortex/frontal cortex. Additionally, they provide increased specificity over the tissue-level in many cases, as illustrated for bipolar disorder[35] with enrichment in both excitatory and inhibitory neuronal subtypes. We further captured certain traits missed in GTEx tissue such as risk tolerance in deep layer excitatory and MGE-like inhibitory neurons, as predicted by Karlsson Linnér, *et al.*[36]. Similarly, we found a strong association between depression and excitatory deep layer neurons, as well as maturing excitatory neurons[37]. We also observed a high enrichment of educational attainment-associated genes in InMGE neurons, concordant with reports of the role of inhibitory neurons in learning and memory[27]. These findings highlight the importance of generating both excitatory and inhibitory neuronal cells within our *in vitro* model.

In addition to brain-related complex traits, iPSC-derived neuronal models are widely used to model rare NDDs, given their ability to recapitulate cell lineages from very early developmental time points and their transcription similarity to fetal, rather than adult cell types. To identify which of our cell types expressed genes associated with NDDs, we evaluated the cell type-specific expression on brain-specific developmental disorder genes from the Deciphering Developmental Disorders (DDD) study[38]. Interestingly, we observed that while approximately 45% of all high-confidence, brain-related DDD genes (n=719) exhibit their highest expression levels in mature neuronal cell types, progenitor cell types also captured another ~30% of genes associated with developmental delay (**Fig. S6c**). Focusing on a subset of DDD genes (n=72) known for their high intolerance to loss-of-function mutations (**Methods**) highlighted the presence of both neuron-specific (e.g., *BCL11A*) and progenitor-specific genes (*PAX6* and *KIF11*) (**Fig. 6c**). This underscores the importance of using temporal models of neurodevelopment in the context of disease research.

Discussion

Transcriptomic data has been hugely informative for human disease genetics studies, providing solid links between genetic variants and transcriptomic features via identification of quantitative trait loci in diverse tissues, cell types, and conditions[39–41]. iPS cells have expanded the range of cell types and lineages available to mapping studies[1,2,39], and made cellular modeling experiments feasible in many traits that affect previously inaccessible cell types. However, since gene expression changes do not always lead to changes in cellular function[42], there is a pressing need to move ‘beyond the transcriptome’ and start linking genetic variants to cell-level phenotypes. This requires well-characterized cellular models and scalable functional assays. To this end, we describe here a comprehensive characterization of iPSC-derived cortical neurons from a widely used protocol where we combined single cell transcriptomics with image-based readouts of cellular morphology. Our study represents a proof-of-concept, where we piloted Cell Painting in a heterogeneous, dynamic system - cortical neurodevelopment - and explored how the joint analysis of imaging and gene expression-based profiles of single cells can contribute to identifying new cellular phenotypes.

A common challenge in modeling cortical neurodevelopment *in vitro*, regardless of the applied protocol, lies in determining whether the cell types generated accurately mirror the transcriptional signatures and developmental trajectories observed *in vivo*. Previous studies in organoids linked *in vitro*-specific cell states to aberrant oxidative or glycolytic stress[4,23]. These alterations in energy-associated pathways are frequently linked to the limitations of the culture media to provide essential nutrients to cells, especially within the necrotic cores of organoids[23]. In a recent study[5], transcriptomic differences between cells from human neural organoids (comprising 26 protocols) and developing human brain (first-trimester)[43] were associated with the upregulation of canonical glycolysis and mitochondrial ATP synthesis-coupled electron transport in organoids. Notably, canonical glycolysis was adopted as a proxy for cell stress given its association with expression differences observed between organoid and primary cells. Similarly, we observed that our low-quality cells showed distinct metabolic and energetic states compared to high-quality cells of the same type. For instance, pathway activation scores differed in glycolysis among progenitors, and in steroids biosynthesis among excitatory neurons. A fraction of these low-quality cells could indeed be linked to an exclusive organoid identity, most of them being either pan-neuronal or pan-radial glial. Mis-annotating these low-quality cells could potentially bias downstream findings if not accounted for.

While scRNA-seq alone allowed us to classify a diverse array of cell types produced, the dynamic nature of developing neurons involves alterations beyond the transcriptome such as in cellular size, shape, and complexity. Cell Painting, with its capacity for large-scale and unbiased screening of cellular morphological phenotypes, proves highly suitable for characterizing an *in vitro* system where phenotypes are not known *a priori*. Furthermore, the application of this assay throughout the developmental trajectory offered insights on the dynamics of morphological readouts, as observed with mitochondrial channel intensity (**Fig. 3b-c**). Analyzing CP readouts presented its own challenges: instead of averaging CP features by well post cell-segmentation, as is often done, we analyzed CP readouts at a single cell level, enabling us to capture morphological heterogeneity, although at the cost of increased noise[44]. Although lower seeding density in culture may improve the accuracy of segmentation, we have previously observed that the viability of developing neurons is compromised in sparser culture conditions.

Given the proof-of-concept nature of this study, the sample size limits our ability to generalize our findings beyond our differentiation. Despite this, donor-specific variation boosted the capacity of the model to link variation in gene expression to CP features. Previous studies have attempted to link gene expression and cell morphology assuming shared biological information between the two, and have found that changes in image-based features are associated with a subset of genes, often related to the cellular components and organelles stained in the assay[10,11]. The generalizability of the CP assay[45] means that such direct links to cellular components are reproducible in different cell lines, such as human osteosarcoma U2OS cell lines used in previous studies versus our neuronal model. For example, we identified functional terms linked to CP features that recapitulate known or expected biology, such as those linked to ER, supporting our model's performance. However, beyond this, morphology-to-gene expression links are likely to be highly cell type-specific, making it difficult to compare findings from U2OS to neuronal cells. To enhance the interpretability of novel associations between features and potential biological function, we applied a linear model rather than a black-box machine learning approach, as in previous cross-modality CP-based approaches[46]. In the future, developing new techniques which systematically link CP readouts with cellular transcriptomes from the same individual cell would offer a ground truth for model validation.

In general, a multi-modal perspective of any system offers insights that may not be visible from any one assay alone. Here, CP revealed donor-specific ER changes corresponding to observed ribosomal transcriptomic differences in inhibitory versus excitatory neurons. Although these two cell types transcriptionally cluster together, the CP cluster marked by the lowest ribosomal association, which likely contains low-ribosome inhibitory neurons, groups amongst progenitors. We thus hypothesize that these observed ribosomal/ER-linked differences could reflect differences in maturity between excitatory and inhibitory neurons. Understanding how interneuron production is altered at the level of both gene expression and cellular processes is key to uncover the mechanisms implicated in NDDs, as suggested by recent findings implicating the ER and cytoskeleton in interneuron development and migration[28]. Further, the production of inhibitory cell types in our *in vitro* system highlights the importance of a human-specific model to recapitulate fetal development, since inhibitory neurons are not known to be produced in the cortex of other model organisms such as mice[17].

Overall, based on our observations, single cell transcriptomics remains a far more in-depth tool for cell type characterization than CP. Indeed, only larger supertypes of cells (progenitors versus neurons) were resolved with the CP assay, potentially due to the generic nature of the dyes being utilized. Replacing generic dyes with those specifically targeting neurons could improve cell type granularity[12], as could increasing image magnification for enhanced resolution of individual organelles. This could help us to better understand low quality cell types within CP data, currently not addressed in our study due to the model limitations. Linked to this, it is also uncertain whether the 384-well format of the CP assay, as compared to 35mm dishes used for scRNA-seq, impacts cell type production.

Finally, we show that our *in vitro* model is relevant to several brain-related traits associated with the cortex, capturing more traits than GTEx brain tissues[34], as expected from the better resolution with cell type-specific expression. In our results, InMGE neurons stand out by capturing the highest number of traits (n=4), with educational attainment being the most significant association. This underscores the vital role of interneurons in maintaining the balance between excitation and inhibition in neural circuits during development, with perturbations of this system having potential implications for processes like learning and memory[27]. Furthermore, we observed distinct temporal and cell-type specific expression of genes associated with developmental disorders in the brain, emphasizing the need to incorporate temporal models in neurodevelopment for disease modeling.

In conclusion, by performing an in-depth characterization study, we have identified which phenotypes can be captured by combining single cell transcriptomics and cell morphology in *in vitro* neuronal systems. This is the first step towards optimization of such a framework that can be extended to genetic or drug perturbation screens[47,48], as the CP assay has been vastly adopted for, or for profiling natural genetic variation[44].

Materials and Methods

Human iPSC culture

The human iPSC lines HEL11.4, HEL47.2, HEL61.1, HEL61.2, HEL62.4 and HEL82.6 used in this study were acquired from the Biomedicum Stem Cell Centre (University of Helsinki, Finland) (**Table 1, S1**). The cells were grown on vitronectin in Essential 8 and Essential 8 Flex media (**Table S5**) at 37°C/5% CO_2. iPSC maintenance in culture was performed according to HipSci guidelines: https://www.culturecollections.org.uk/media/109442/general-guidelines-for-handling-hipsci-ipscs.pdf). Cells were clump-passaged in ratios ranging from 1:4 to 1:8 using 0.5 mM EDTA diluted in DPBS-/-. Y-27632 (10 µM) was used for better cell survival at thawing. Cells were tested for mycoplasma with the MycoAlert kit, and all lines tested negative after thawing both during iPS cell culture and neural differentiation.

Cortical neuron differentiation

The iPSC lines were differentiated into cortical progenitors and neurons using an established differentiation protocol[6] with minor modifications (hereafter referred to as 'original') and a modified version from day 11 post-induction (**Table S2**).

For neural inductions, 2-3 80% confluent plates of iPS cells were detached using 0.5 mM EDTA and were plated on a Matrigel plate (1:100 in DMEM/F12) in E8 medium supplemented with Y-27632 (10 µM). Dual-SMAD inhibition was initiated the following day using Neural Maintenance Medium (NMM) supplemented with SB431542 (10 µM) and LDN-193189 (200 nM) (**Table S5**). On day 11 post-induction, cells were split in clumps in 1:2 ratio onto laminin-coated dishes using either mechanical dissociation by gentle scraping (modified) or using Dispase (original). The following day, the media was changed to NMM containing bFGF (0.2 µg/ml) for four days. After expansion, cells were split (1:2) with EDTA only in the modified protocol. Alternatively, a few replicates (techRep column, **Table S2**) for days 40 and 70 were dissociated with Dispase as per the original protocol.

At day 17, the plates to be assayed at day 20 (modified protocol) were split 1:2 as small clumps (using 0.5 µM EDTA) onto laminin-coated plates for scRNA-seq analysis. Additionally, cells were plated in 1:6 ratio on 24-well plates with coverslips for immunocytochemistry and in 1:120 ratio on 384-well plates for Cell Painting. Cells assayed at days 40 and 70 were split as described in **Table S2**.

All cells were frozen down at day 28 or 29 and thawed as per the original protocol. Cells were frozen down in 1:1 ratio and were plated onto laminin-coated plates at thawing. Final plating for days 40 and 70 was done at day 35 when cells were passaged with Accutase. Cells were plated for scRNA-seq (1.5 million cells/35mm dish), immunocytochemistry (75-300,000 cells/24-well plate) and Cell Painting (5,000 cells/384-well plate) onto poly-L-ornithine and laminin-coated plates. Poly-L-ornithine solution was diluted to 0.01% with sterile water, coated overnight at +4°C after which the wells were washed 3 times with sterile water. Laminin was diluted in DPBS-/- and the plates were incubated at 37°C for 4h.

scRNA-seq samples profiled at days 20, 40 and 70 were not taken from the same continuous differentiation. Days 40 and 70 were sampled from one round of differentiation, containing 4 donors (HEL61.2, HEL11.4, HEL62.4, HEL82.6) and with technical replicates as specified in **Table S3**. An additional round of differentiation was run to profile Cell Painting samples in all three time points, and in addition, day 20 scRNA-seq samples were obtained from this batch. These samples were only differentiated using the modified version of the protocol. This time point incorporated two additional iPSC lines, HEL61.1 (clone of HEL61.2) and HEL47.2 (derived from the same donor as HEL11.4, but generated from different parental fibroblasts), requiring the barcoding technology of CellPlex to demultiplex donor identity. For this time point, two independent inductions were replicated one week apart (batchRep column, **Table S3**).

Cell preparation for single cell RNA sequencing

Developing cortical neurons were analyzed for experiments on days 20, 40 and 70 post neural induction. The cells were prepared for scRNA-seq as follows: The wells were washed up to three times with DPBS-/- after which they were incubated in Accutase for 5 min at 37°C. Cells were dissociated into a single cell suspension by pipetting and added into 5 ml of 0.04% BSA in DPBS-/-. Cells were centrifuged at 180 RCF for 5 min and supernatant was removed. Cells were resuspended in 0.04% BSA and centrifuged twice more. Final resuspension of cells was done in 100 μl of 0.04% BSA after which the cells were filtered through 40 μm FlowMe filters, followed by counting and estimation of the cell viability using Trypan Blue.

Single-cell RNA-sequencing library chemistry and sequencing

Single-cell gene expression was profiled from the three time points using 10x Genomics Chromium Single Cell 3' Gene Expression technology. Only at day 20, Cell Multiplexing technology platform (3' CellPlex Kit) was used to demultiplex the identity of clonal cell lines. For all the time points, 10x libraries were generated using the Chromium Next GEM Single Cell 3' Gene Expression version 3.1 Dual Index chemistry. The sample libraries were sequenced on Illumina NovaSeq 6000 system using read lengths: 28bp (Read 1), 10bp (i7 Index), 10bp (i5 Index) and 90bp (Read 2) (**Table S4**).

Genotyping

To allow for donor demultiplexing during downstream analysis, iPSC lines were genotyped using SNP arrays. For this, cells were pelleted in DPBS-/- and DNA was extracted using Nucleospin DNA columns. Genotyping was performed on Illumina Global Screening Array with added GSAFIN SNPs specific for the Finnish population.

Immunocytochemistry and image acquisition

Cells were washed three times with DPBS+/+, fixed with 4% paraformaldehyde for 15 min followed by three DPBS washes. Cells were then permeabilized in 0.2% Triton X-100/DPBS for 15 min at RT (**Table S5**). Coverslips were washed three times in PBST (0.1% Tween-20) followed by blocking at RT with 5% BSA/PBST for two hours. Cells were incubated in primary antibody in 5% BSA/PBST overnight at 4°C (**Table S6**). Following overnight incubation, coverslips were washed with PBST for 15 min three times, followed by incubation in secondary antibody in 5% BSA/PBST for one hour. The cells were finally washed three times with DPBS for 10 min and coverslips were plated on glass slides with mounting media containing DAPI. Fixation for lines HEL62.4 and HEL82.6 was performed on day 55 rather than day 70 due to neuron detachment from the coverslips.

Imaging for day 20 ICC was performed using a Zeiss Axio Observer.Z1. The objective used was a Plan-Apochromat NA 0.8 at 20x magnification. Samples were imaged with HXP 120V light source with the 45 Texas Red, 38HE GFP and 49 DAPI wavelength fluorescence filters. Images were acquired using an Axiocam 506. For days 40 and 70, imaging was performed using a Zeiss Axio Imager 1 with the same objective and light source. Fluorescence filters used were 64HE mPLum, 38HE GFP and 49 DAPI. Images were acquired using a Hamamatsu Orca Flash 4.0 LT B&W.

Cell Painting assay and image acquisition

Cells were phenotyped using Phenovue Cell Painting Kit for 384-well plates following kit guidelines based on[9]. Cells were plated on day 17 (for day 20) or day 35 (for days 40 and 70) on PhenoPlate 384-well microplates and incubated in 37°C at 5% CO_2 until assay time points at days 20, 40 and 70. Staining solution 1 was added for live labeling of mitochondria (PhenoVue 641 Mitochondrial Stain) and incubated in the dark for 30 min at 37°C. Cells were fixed with 3.2% PFA for 20 min at room temperature, and then were washed and incubated with 0.1% Triton X-100 followed by HBSS washes. Finally, staining solution 2 was added to the cells to label nuclei (PhenoVue Hoechst 33342 Nuclear Stain), ER (PhenoVue Fluor 488 - Concanavalin A), Golgi apparatus (PhenoVue Fluor 555 - WGA), nucleic acid (PhenoVue 512 Nucleic Acid Stain) and cytoskeleton (PhenoVue Fluor 568 - Phalloidin) and washed again with HBSS prior to imaging.

The cells were imaged with PerkinElmer Opera Phenix High Content Screening System using the Harmony Software v4.9. The imaging was done using the 40x NA 1.1 water immersion object and with the following lasers: 405 nm (emission window 435-480 nm), 488 nm (500-550 nm), 561 nm (570-630 nm), and 640 nm (650-760 nm), resulting in Golgi apparatus, nucleic acid and cytoskeletal dyes being captured in the same channel (CGAN). Images were captured using the Andor Zyla sCMOS camera (2160 x 2160 pixels; 6.5 µm pixel size). For each well, 28 fields on 3 planes were acquired. Amongst images taken from multiple planes (n=3), the z-stack with the highest intensity per channel was selected for analysis.

scRNA-seq data pre-processing and dimensional reduction

Raw data processing and analysis were performed using 10x Genomics Cell Ranger v6.1.2 pipelines “cellranger mkfastq” to produce FASTQ files and “cellranger multi” to perform alignment, filtering and UMI counting. mkfastq was run using the Illumina bcl2fastq v2.2.0 and alignment was done against human genome GRCh38. Day 20 samples were demultiplexed based on multiplexing barcode sequences using the cellranger multi pipeline. Cell recovery was 22,628 and 18,486 from the two 10x samples sequenced, with 50.89% and 73.61% cells assigned to a cell line (singlet rate), respectively, resulting in approximately 4,000 cells captured per cell line across technical replicates (**Table S4**). In 10x samples from days 40 (n=3) and 70 (n=2), donors were pooled at the time of sequencing. We assigned donor identity to each cell with *demuxlet*[49] by leveraging common genetic variation from the same donors previously genotyped (see Methods, Genotyping section). *Demuxlet* was run using a default prior doublet rate of 0.5. We only retained those (singleton) cells that could unambiguously be linked to a donor (average of 69.5% per pool), resulting in 5,011 cells on average per donor at each timepoint.

scRNA-seq data was analyzed using the *Seurat* R package v4.1.1 (Stuart et al., 2019) using R v4.1.3. To exclude low-quality cells from analysis, we discarded cells with either less than 2,000 genes expressed or more than 8,000, as well cells presenting more than 15% of reads mapping to the mitochondrial DNA. Additionally, it was ensured that each 10x sample contained between 10-20% reads mapping to ribosomal protein transcripts on average, as expected from neuronal populations. Following filtering, the 10x samples from all three timepoints were merged and genes expressed in <0.1% of cells in the merged dataset were removed.

Gene expression counts were normalized by total expression, with a default scale factor of 10,000, and then transformed to log-space. Then, this matrix of log-normalized counts was scaled while regressing out cell cycle scores[50], depicted as the difference between G2/M and S phase scores to preserve inherent differences between cycling and non-cycling cells. Dimensionality reduction was performed via Principal Component Analysis (PCA) using previously identified highly variable genes (n=3,000). *Harmony* (v.0.1.0) was used to batch-correct the PCA embeddings from all 10x samples[51]. Based on the top 15 batch-corrected PCs, we constructed a KNN graph and clustered the cells with a resolution of 0.8, using Seurat functions *FindNeighbors()* and *FindClusters()*, respectively. We then generated a UMAP embedding again using the top 15 batch-corrected PCs from *Harmony*.

scRNA-seq cell type annotations from *in vivo* fetal brain

The primary reference dataset used for cell type annotation was the publicly available human fetal scRNA-seq data from Poulioudakis et al.[16], obtained from the CoDEx online interface (http://solo.bmap.ucla.edu/shiny/webapp/). It was selected given the data and code availability, plus the metadata with regional specificity of the developing neocortex. The raw matrix of counts was log-normalized to a scale factor of 10,000 counts and we identified the top 3,000 highly variable genes. Based on the expression of G2/M and S phase markers, we calculated cell cycle phase scores. Then, counts were scaled, regressing out ‘Number_UMI’, ‘Library’ and ‘Donor’ and the difference between G2/M and S cell cycle scores. Dimensionality reduction was performed via PCA on the top 3,000 highly variable genes. We then batch-corrected the PCA embeddings with Harmony specifying the library as a covariate and used the harmonized dimensional reduction as an embedding to project our *in vitro* dataset. To transfer the cell type labels from the fetal reference to our *in vitro* query dataset, we used a two-step anchor-based approach implemented in Seurat: first running ‘FindTransferAnchors’ using the first 30 batch-corrected PCA from the reference embedding, and then “MapQuery”. Further, the tag of ‘Unmapped’ was assigned to cells that did not achieve a mapping score of >0.5 for any cell type label. Correlation analysis of the annotated cell types between the *in vitro* and reference datasets was performed similar to Bhaduri *et al.* (2020)[4]. On-diagonal and off-diagonal means of Pearson correlation coefficient were calculated. We classified cells in bins of low and high quality within a cell type assigned based on their best mapping score. Those cells with a score>0.5 were referred to as high quality for a predicted cell type, while cells with a score<0.5 were considered as low-quality cells. Additionally, cell types with less than 50 cells were not considered for any downstream per-cell type analyses (in this case, only ExDp2).

Pseudotime analysis

The pseudotime trajectory was constructed using R package *monocle3* (v1.2.9). The Seurat object was converted to the *monocle3*-compatible cds object type using the function ‘*as.cell_data_set()*’ followed by pre-processing with 100 dims, alignment by 10x sample and clustering at a resolution of 1e-4. The ‘*learn_graph()*’ function was used with default parameters to construct the trajectory and the cells were ordered along the trajectory using a principal node rooted in the time point day 20. Genes that vary across the trajectory were identified using '*graph_test()*' by setting the argument '*neighbor_graph" to "principal_graph*". The resulting genes were grouped into modules based on '*find_gene_modules()*' after evaluating modularity using different resolution parameters {10^{-6}, 10^{-5}, 10^{-4}, 10^{-3}, 10^{-2}, 10^{-1}}.. Finally, the expression of these modules was aggregated per cell type using the function '*aggregate_gene_expression()*'.

GO enrichment

Overrepresentation analysis using gene ontology (GO)[52] was performed using *clusterProfiler* v4.2.2 and *org.Hs.eg.db* v3.14.0. The gene universe consists of 23,289 genes present after filtering out those expressed in <0.1% of cells (see Methods, scRNA-data pre-processing), and mapped to ENTREZ and ENSEMBL gene IDs. The *enrichGO* function from *clusterProfiler* was used to find enriched terms of all categories ('BP', 'CC' and 'MF') per previously identified gene module and top 15 terms per analysis (passing a qvalueCutoff=0.05) were visualized using *enrichplot* v1.14.2.

GSVA

Gene expression was aggregated per cell type based on mean log-normalized expression values to generate pseudobulked data. Gene set variation analysis was performed on pseudobulked cell types using the R package *GSVA* v1.49.4 and gene sets obtained from the Molecular Signatures Database (MSigDB)[53] compiled in the R package *msigdbr* v7.5.1. Selected pathways from KEGG (**Fig. 3d & 5c**) or Gene Ontology: Cellular Components (GO CC) containing the 'MITOCHONDRIAL' term (**Fig. 3e**) were tested for enrichment across cell types using the function 'gsva' with a min.sz filter of 15 and max.sz of 500.

Organoid mapping

Reference scRNA-seq data from cortical organoids was obtained from Bhaduri et al.[4], via the UCSC Cell Browser (https://cells.ucsc.edu/?ds=organoidreportcard). As in the original publication, the raw count matrix was pre-processed following original filtering steps to remove cells with fewer than 500 genes expressed or with an excessive mitochondrial count fraction (>10%). Then, gene counts were normalized to a scale factor of 10,000 counts and natural-log transformed and computed the 3,000 highly variable genes. Based on the expression of G2/M and S phase markers, we calculated cell cycle scores, and the difference between G2/M and S was regressed out during data scaling. We performed PCA dimensionality reduction using the top 3,000 highly variable genes. We used the first 30 PCA to project the organoid reference to our in vitro dataset as described for fetal mapping. This reference mapping was the second step in producing the final cell type annotation, as we only assigned the organoid cell type labels to those cells that were classified as 'unmapped' from the fetal reference-based (first-step annotation). Those cells that did not achieve a maximum mapping score of >0.5 for any cell type label in any of the two mappings were finally tagged as "Unmapped".

Differential abundance testing

We tested for differential abundance between the cell types produced by the two versions of the protocol (original vs modified) using *miloR* v1.4.0[24]. This analysis was performed solely with samples from day 40 due to the representation of all donors in each protocol version (**Table S2**). The KNN graph was constructed using the *buildGraph()* function with 15 dimensions (d=15) and 30 nearest-neighbors (k=30), followed by *makeNhoods()* using the same number of dimensions and sampling 20% of the graph vertices (prop=0.2). In both cases, the dimensionality reduction from Harmony after batch-correcting the PCA was used. To calculate the distance between neighborhoods, we used the function *calcNhoodDistance()* with 15 dimensions (d=15) from Harmony. The neighborhoods were tested for differential abundance between protocols by running *testNhoods()* with the design:

~ donor + protocol

The resulting differentially abundant neighborhoods were annotated with cell types from the two-step annotation using *annotateNhoods()*, and neighborhoods that were not homogeneously composed of a single cell type (fraction of cells from any given cell type <0.7) were annotated as 'Mixed'. The differential abundance fold changes were visualized using a beeswarm plot with default significance level for Spatial FDR (<0.1).

Gene Set Enrichment Analysis (GSEA)

GSEA was performed on differentially expressed genes between pan-neuronal and inhibitory cell types (**Fig. 4d**) or between excitatory and inhibitory cell types (**Fig. 5b, S5c**) using *fgsea* v1.20.0. The function 'fgseaMultilevel' was used on the ranked list of DEGs using KEGG gene sets from msigdbr and filtering for minsize=10, maxsize=500, eps=0 and nPErmSimple=10000. Results were ordered by NES and filtered for padj<0.05 before visualizing the top (maximum) 20 results per analysis. Additionally, in sections 4 & 5, the genes driving specific pathways were identified based on the 'leadingEdge' of each pathway and represent the core of the gene set enrichment's signal[20,21]. The module score for each of these core sets of genes was computed per single cell using 'AddModuleScore' from *Seurat* with default parameters.

Cell Painting image processing

The acquired images were processed using *CellProfiler* 4.2.1[54]. The workflow file is available in the article Github at CellPainting/cellProfilerWorkflow.cppipe. Briefly, quality metrics such as blurriness and saturation were measured for each image. Nuclei were then segmented using the Hoechst channel using the minimal cross-entropy method. Then, an image summing up the channels and excluding Nucleus staining was generated to segmentate the cells (**Supplementary Methods Fig. 1a**). Neurites were algorithmically enhanced on summed images prior to segmentation. Cell segmentation was done by propagation from the nucleus using the Otsu method. Cytoplasms were identified by subtracting nuclei area to the cell. For each object type (Cell, Nuclei, Cytoplasm), a large number of features were measured per channel. A description of each feature can be found in the CellProfiler manual (https://cellprofiler-manual.s3.amazonaws.com/CellProfiler-4.0.4/help/). Those features were metrics relative to channel intensity, texture or object shape and size. To export images, intensity of each channel was rescaled and attributed to a color. Channels merged to create one image per field in the well. An overlay of the well is then created for each field using a python script.

Analysis of quantified features of Cell Painting

The feature data frames were analyzed by R 4.2 using the *oob* package (https://github.com/DimitriMeistermann/oob). First, images underwent a filtering process based on the PowerLogLogSlope, a blur metric. For each field, the average PowerLogLogSlope was calculated across the four channels. We retained images with an average value greater than -2.16, which is determined based on the distribution. Additionally, images identified as blurry by Cell Profiler are excluded. Any objects associated with discarded images are removed from the dataset. Cells exhibiting extreme values for cytoplasm area (≤1000 or ≥100000) or too small nucleus (≤10000) are also eliminated, as they are indicative of poor segmentation. Cells with too low nucleus channel intensity were also excluded (≤0.003), as well as being outlier in a projection with nucleus intensity as x-axis and sum of other channels as y-axis. Outliers were determined by a uniform kernel density estimation with bandwidth=1 and removed if density ≤0.0001.

Features were then regularized to approximately follow a normal distribution. This was done by examining each feature distribution and classifying them. We defined 6 feature distribution families (**Supplementary Methods Fig. 8, Supplementary Methods Table 1**) and applied a specific transformation for each. For example, intensity features underwent a log2(x+1) transformation. Range of each feature was then scaled to [0,1000].

The dataset, originally containing 1,186,458 cells, was reduced for ensuring a relatively balanced contribution from each experimental population (time-point × cell line) and reducing the computation time. The subsampling was aimed to reach a range of 50,000 to 60,000 cells. This specific range was determined using bootstrapping, which involved repeatedly sampling the dataset and assessing the correlation between the subsamples and the original dataset. When 50,000 cells were selected, the average correlation was approximately 0.98. Subsampling was carried out based on experimental populations, considering differentiation day and cell line, with a maximum of 2000 cells drawn if the population exceeded this size.

Feature selection was conducted through a multi-step process. Initially, a feature graph was constructed, and edges were established between features if their correlation exceeded 0.99. Modules were subsequently identified from this graph using the function "cluster_fast_greedy" from the *igraph* package[55]. Within each of these modules, the most parsimonious feature was retained for further analysis. The features associated with spatial measures (x-y locations), Zernike-related values, and Cel_Neighbors_AngleBtNghbors_Adjacent were excluded from further analysis. Their signals did not exhibit a discernible pattern and, as a result, posed a potential risk of introducing noise into subsequent analyses.

Finally, a temporary cell clustering was performed (see next paragraph), and the pictures of cells from each cluster was assessed, revealing two clusters composed of image artifacts or dying cells. Those clusters were removed from downstream analysis. We obtained a feature matrix consisting of 223 features and 54,415 cells.

A UMAP and Leiden clustering analysis was conducted using the *oob* package with a specified parameter of "n_neighbors = 20." Subsequently, feature modules were identified by performing hierarchical clustering on the features, utilizing a covariance distance matrix. The number of modules was determined using the derivative loss method. This process resulted in the identification of a total of 18 modules, and they were named based on an examination of their content. To determine module activation scores, the first component of a Principal Component Analysis (PCA) was extracted from the matrix, which contained the features of each module for all cells. The web interface for visualizing the CP dataset was coded using the d3.js framework.

Integration of scRNA-Seq and Cell Painting

For the purpose of the multi-modal analysis, scRNA-seq data was reprocessed to enhance comparability between CP features and gene expression, aiming to align these datasets as closely as possible. The used set of cells is consistent with those used in the primary scRNA-seq analyses (refer to the section on scRNA-seq data pre-processing for more details). The genes with average expression < 0.005 were filtered out and normalization was performed using the computeSumFactors function from *scran*[56]. Batches were corrected using fastMNN with k=5 from the *batchelor* package[57].

To perform the integration, only the common experimental population (combination of differentiation day and cell line) were selected, then 3 metacells were created per experimental population per modality. The metacells were created by randomly attributing cells from each experimental population to one of three metacell. Feature values or gene expressions were then averaged by metacell. This led to 2 matrices of 42 metacells. These matrices were used to train Lasso regressions models using *sklearn*[58] from Python (alpha=0.02, max_iter = 10000). For each experimental population, two metacells from each modality were used for the training and one for cross-validation. The intercepts and regression coefficients were then exported to a matrix that was used to predict CP features from gene expression. This matrix was used to build the predicted Cell Painting feature matrix of the scRNA-Seq dataset. CP features markers of each CP cluster were computed in the CP feature matrix, and CP features markers of each cell type in the predicted CP feature matrix. This was done using getMarkers from the *oob* package. Subsequently, two marker score matrices were generated and correlated to obtain **Fig. 2e**.

Parallelly to the lasso regression models, regular linear regressions were computed with the same formula (*CP feature ~ genes*) with the aim to provide one value per gene for each CP feature. This enabled the use of GSEA to enrich CP features, using the regression coefficients as GSEA input scores. Prior to the enrichment, a median of coefficients was computed per CP module to perform the enrichment per module with KEGG and GO databases as gene set databases.

For each cell from the scRNA-Seq dataset, the predicted CP feature matrix was used along the Seurat cell cycle scores annotation to build two lasso regression models: one to predict S.score, the other to predict the G2M score with a formula on the form of *score ~ CP features*. The models were then used to predict the cell cycle scores values in the CP dataset.

AMI

Adjusted Mutual Information (AMI) was computed using the *aricode* package for R[59].

Stratified linkage disequilibrium (LD) score regression analysis

Positive markers per annotated cell type from our *in vitro* dataset were determined using *Seurat FindMarkers()* function. A 100 kb window was added on either side of each of these genes using the GenBank reference genome version NCBI:GCA_000001405.14 from GRCh37.p13 (https://ftp.ensembl.org/pub/grch37/current/fasta/homo_sapiens/pep/) and LD scores computed. We then investigated heritability enrichment for 79 traits (**Table S7**) given our cell-type specific annotations (n=22 cell types) using stratified LD score regression implemented in LDSC (*LDSC* v1.0.0)[33], with the full set of genes expressed in at least <0.1% of cells (n=23,289) as the control gene set. As a comparison, we ran the same analysis using annotations for 13 brain tissues from GTEx[34]. Multiple testing correction was performed across resulting trait-specific p-values across all cell/tissue types using the Benjamini-Hochberg Procedure.

Expression of brain-related developmental delay genes

Developmental delay associated genes from the DDD study were obtained from https://www.ebi.ac.uk/gene2phenotype (version 28_7_2023). The geneset was filtered for loss of function (absent gene product) brain-specific genes of ‘definitive’ confidence and with autosomal monoallelic requirement. Finally, genes were filtered for loss-of-function observed/expected upper bound fraction (LOEUF) score <0.3 in order to limit the analysis to genes with higher probability of large consequence on cellular phenotypes. LOEUF information was downloaded from gnomAD v4[60]. The selected genes’ scaled expression was plotted per pseudobulked cell type from the fetal annotation.

Data availability

Raw scRNA-seq data and genotype information from the cell lines used in the *in vitro* cortical differentiation will be made available on the European Genome-Phenome Archive. Additionally, raw image data from CP will be deposited to the EMBL-EBI BioImage Archive. Count matrices and metadata from both scRNA-seq and CP, as well as the CP-to-gene expression coefficient matrix and functional enrichment of CP feature modules, will be made available in Zenodo.

Code availability

Code used to analyze the scRNA-seq and Cell Painting datasets is available at https://github.com/Kilpinen-group/cortical_diff_code/. Additionally, an online interface linking the CP UMAP to individual images to facilitate exploration of the CP dataset will be made available.

Acknowledgements

This work was primarily funded by the Helsinki Institute of Life Science (HiLIFE), University of Helsinki (UH). We also acknowledge additional financial support from the Doctoral Programme in Integrative Life Science, UH (AS), Maud Kuistila Memorial Foundation (RW), and the Sigrid Juselius Foundation (HK, PPC). The cell lines used in this study were obtained from the Biomedicum Stem Cell Center (BSCC), supported by HiLIFE and Biocenter Finland. Genotyping was performed at the Institute for Molecular Medicine Finland FIMM Genomics unit, supported by HiLIFE and Biocenter Finland. The authors would like to thank the FIMM Single-Cell Analytics unit, supported by HiLIFE and Biocenter Finland, for single-cell RNA-sequencing services, and Dr. Lassi Paavolainen and the FIMM High Content Imaging and Analysis unit for assistance with Cell Painting and for imaging and image data analysis. Imaging for ICC was performed at the Biomedicum Imaging Unit, Helsinki University, Helsinki, Finland, with the support of Biocenter Finland. The authors also wish to acknowledge CSC – IT Center for Science, Finland, for computational resources, and Dr. Lewis Evans for providing feedback on the manuscript.

Declaration of interests

The authors declare no competing interests.

References

1. Jerber, J. *et al.* Population-scale single-cell RNA-seq profiling across dopaminergic neuron differentiation. *Nat. Genet.* 53, 304 (2021).
2. Kilpinen, H. *et al.* Common genetic variation drives molecular heterogeneity in human iPSCs. *Nature* 546, 370 (2017).
3. Volpato, V. *et al.* Reproducibility of Molecular Phenotypes after Long-Term Differentiation to Human iPSC-Derived Neurons: A Multi-Site Omics Study. *Stem Cell Reports* 11, 897–911 (2018).
4. Bhaduri, A. *et al.* Cell stress in cortical organoids impairs molecular subtype specification. *Nature* 578, 142–148 (2020).
5. He, Z. *et al.* An integrated transcriptomic cell atlas of human neural organoids. *bioRxiv* 2023.10.05.561097 (2023) doi:10.1101/2023.10.05.561097.
6. Shi, Y., Kirwan, P. & Livesey, F. J. Directed differentiation of human pluripotent stem cells to cerebral cortex neurons and neural networks. *Nature Protocols 2012 7:10* 7, 1836–1846 (2012).
7. Shi, Y., Kirwan, P., Smith, J., Robinson, H. P. C. & Livesey, F. J. Human cerebral cortex development from pluripotent stem cells to functional excitatory synapses. *Nat. Neurosci.* 15, 477–486 (2012).
8. Gustafsdottir, S. M. *et al.* Multiplex cytological profiling assay to measure diverse cellular states. *PLoS One* 8, e80999 (2013).
9. Bray, M.-A. *et al.* Cell Painting, a high-content image-based assay for morphological profiling using multiplexed fluorescent dyes. *Nat. Protoc.* 11, 1757–1774 (2016).
10. Haghighi, M., Caicedo, J. C., Cimini, B. A., Carpenter, A. E. & Singh, S. High-dimensional gene expression and morphology profiles of cells across 28,000 genetic and chemical perturbations. *Nat. Methods* 19, 1550–1557 (2022).
11. Nassiri, I. & McCall, M. N. Systematic exploration of cell morphological phenotypes associated with a transcriptomic query. *Nucleic Acids Res.* 46, e116 (2018).
12. Laber, S. *et al.* Discovering cellular programs of intrinsic and extrinsic drivers of metabolic traits using LipocyteProfiler. *Cell Genom* 3, 100346 (2023).
13. Handel, A. E. *et al.* Assessing similarity to primary tissue and cortical layer identity in induced pluripotent stem cell-derived cortical neurons through single-cell transcriptomics. *Hum. Mol. Genet.* 25, 989 (2016).
14. van de Leemput, J. *et al.* CORTECON: A Temporal Transcriptome Analysis of In Vitro Human Cerebral Cortex Development from Human Embryonic Stem Cells. *Neuron* 83, 51–68 (2014).
15. Hao, Y. *et al.* Integrated analysis of multimodal single-cell data. *Cell* 184, 3573–3587.e29 (2021).
16. Polioudakis, D. *et al.* A Single-Cell Transcriptomic Atlas of Human Neocortical Development during Mid-gestation In Brief. *Neuron* 103, 785–801 (2019).
17. Delgado, R. N. *et al.* Individual human cortical progenitors can produce excitatory and inhibitory neurons. *Nature* 601, 397–403 (2022).
18. Stuart, T. *et al.* Comprehensive Integration of Single-Cell Data. *Cell* 177, 1888–1902.e21 (2019).
19. Zhang, S., Zhao, J., Quan, Z., Li, H. & Qing, H. Mitochondria and Other Organelles in Neural Development and Their Potential as Therapeutic Targets in Neurodegenerative Diseases. *Front. Neurosci.* 16, 853911 (2022).
20. Mootha, V. K. *et al.* PGC-1alpha-responsive genes involved in oxidative phosphorylation are

coordinately downregulated in human diabetes. *Nat. Genet.* 34, 267–273 (2003).
21. Subramanian, A. *et al.* Gene set enrichment analysis: a knowledge-based approach for interpreting genome-wide expression profiles. *Proc. Natl. Acad. Sci. U. S. A.* 102, 15545–15550 (2005).
22. Romero-Morales, A. I. & Gama, V. Revealing the Impact of Mitochondrial Fitness During Early Neural Development Using Human Brain Organoids. *Front. Mol. Neurosci.* 15, 840265 (2022).
23. Uzquiano, A. *et al.* Proper acquisition of cell class identity in organoids allows definition of fate specification programs of the human cerebral cortex. *Cell* 185, 3770–3788.e27 (2022).
24. Dann, E., Henderson, N. C., Teichmann, S. A., Morgan, M. D. & Marioni, J. C. Differential abundance testing on single-cell data using k-nearest neighbor graphs. *Nature Biotechnology 2021 40:2* 40, 245–253 (2021).
25. Contractor, A., Ethell, I. M. & Portera-Cailliau, C. Cortical interneurons in autism. *Nat. Neurosci.* 24, 1648–1659 (2021).
26. Paulsen, B. *et al.* Autism genes converge on asynchronous development of shared neuron classes. *Nature* 602, 268–273 (2022).
27. Ramamoorthi, K. & Lin, Y. The contribution of GABAergic dysfunction to neurodevelopmental disorders. *Trends Mol. Med.* 17, 452–462 (2011).
28. Meng, X. *et al.* Assembloid CRISPR screens reveal impact of disease genes in human neurodevelopment. *Nature* 622, 359–366 (2023).
29. Alzu'bi, A. *et al.* The Transcription Factors COUP-TFI and COUP-TFII have Distinct Roles in Arealisation and GABAergic Interneuron Specification in the Early Human Fetal Telencephalon. *Cereb. Cortex* 27, 4971–4987 (2017).
30. Strano, A., Tuck, E., Stubbs, V. E. & Livesey, F. J. Variable Outcomes in Neural Differentiation of Human PSCs Arise from Intrinsic Differences in Developmental Signaling Pathways. *Cell Rep.* 31, 107732 (2020).
31. Zhang, Y. *et al.* Cortical Neural Stem Cell Lineage Progression Is Regulated by Extrinsic Signaling Molecule Sonic Hedgehog. *Cell Rep.* 30, 4490–4504.e4 (2020).
32. Wynne, M. E. *et al.* Heterogeneous Expression of Nuclear Encoded Mitochondrial Genes Distinguishes Inhibitory and Excitatory Neurons. *eNeuro* 8, (2021).
33. Finucane, H. K. *et al.* Heritability enrichment of specifically expressed genes identifies disease-relevant tissues and cell types. *Nat. Genet.* 50, 621–629 (2018).
34. GTEx Consortium. The Genotype-Tissue Expression (GTEx) project. *Nat. Genet.* 45, 580–585 (2013).
35. Skene, N. G. *et al.* Genetic identification of brain cell types underlying schizophrenia. *Nat. Genet.* 50, 825–833 (2018).
36. Karlsson Linnér, R. *et al.* Genome-wide association analyses of risk tolerance and risky behaviors in over 1 million individuals identify hundreds of loci and shared genetic influences. *Nat. Genet.* 51, 245–257 (2019).
37. Nagy, C. *et al.* Single-nucleus transcriptomics of the prefrontal cortex in major depressive disorder implicates oligodendrocyte precursor cells and excitatory neurons. *Nat. Neurosci.* 23, 771–781 (2020).
38. Wright, C. F. *et al.* Genetic diagnosis of developmental disorders in the DDD study: a scalable analysis of genome-wide research data. *Lancet* 385, 1305–1314 (2015).
39. Cuomo, A. S. E., Nathan, A., Raychaudhuri, S., MacArthur, D. G. & Powell, J. E. Single-cell genomics meets human genetics. *Nat. Rev. Genet.* 24, 535–549 (2023).
40. Umans, B. D., Battle, A. & Gilad, Y. Where Are the Disease-Associated eQTLs? *Trends Genet.* 37, 109–124 (2021).
41. Kundu, K. *et al.* Genetic associations at regulatory phenotypes improve fine-mapping of causal variants for 12 immune-mediated diseases. *Nat. Genet.* 54, 251–262 (2022).
42. El-Brolosy, M. A. & Stainier, D. Y. R. Genetic compensation: A phenomenon in search of mechanisms. *PloS Genet.* 13, e1006780 (2017).
43. Braun, E. *et al.* Comprehensive cell atlas of the first-trimester developing human brain. *Science* 382, eadf1226 (2023).
44. Caicedo, J. C. *et al.* Cell Painting predicts impact of lung cancer variants. *Mol. Biol. Cell* 33, ar49 (2022).
45. Willis, C., Nyffeler, J. & Harrill, J. Phenotypic Profiling of Reference Chemicals across Biologically Diverse Cell Types Using the Cell Painting Assay. *SLAS Discov* 25, 755–769 (2020).

46. Way, G. P. *et al.* Predicting cell health phenotypes using image-based morphology profiling. *Mol. Biol. Cell* 32, 995–1005 (2021).
47. Way, G. P. *et al.* Morphology and gene expression profiling provide complementary information for mapping cell state. *Cell Syst* 13, 911–923.e9 (2022).
48. Chandrasekaran, S. N. *et al.* JUMP Cell Painting dataset: morphological impact of 136,000 chemical and genetic perturbations. *bioRxiv* 2023.03.23.534023 (2023) doi:10.1101/2023.03.23.534023.
49. Kang, H. M. *et al.* Multiplexed droplet single-cell RNA-sequencing using natural genetic variation. *Nat. Biotechnol.* 36, 89–94 (2018).
50. Tirosh, I. *et al.* Single-cell RNA-seq supports a developmental hierarchy in human oligodendroglioma. *Nature* 539, 309–313 (2016).
51. Korsunsky, I. *et al.* Fast, sensitive and accurate integration of single-cell data with Harmony. *Nat. Methods* 16, 1289–1296 (2019).
52. Gene Ontology Consortium *et al.* The Gene Ontology knowledgebase in 2023. *Genetics* 224, (2023).
53. Liberzon, A. *et al.* Molecular signatures database (MsigDB) 3.0. *Bioinformatics* 27, 1739–1740 (2011).
54. Stirling, D. R. *et al.* CellProfiler 4: improvements in speed, utility and usability. *BMC Bioinformatics* 22, 433 (2021).
55. Creators Csárdi, Gábor Nepusz, Tamás Müller, Kirill Horvát, Szabolcs Traag, Vincent Zanini, Fabio Noom, Daniel. *igraph for R: R interface of the igraph library for graph theory and network analysis*. Doi:10.5281/zenodo.8240644.
56. Lun, A. T. L., McCarthy, D. J. & Marioni, J. C. A step-by-step workflow for low-level analysis of single-cell RNA-seq data with Bioconductor. *F1000Res.* 5, 2122 (2016).
57. Haghverdi, L., Lun, A. T. L., Morgan, M. D. & Marioni, J. C. Batch effects in single-cell RNA-sequencing data are corrected by matching mutual nearest neighbors. *Nat. Biotechnol.* 36, 421–427 (2018).
58. Pedregosa, F. *et al.* Scikit-learn: Machine Learning in Python. *J. Mach. Learn. Res.* 12, 2825–2830 (2011).
59. Sundqvist, M., Chiquet, J. & Rigaill, G. Adjusting the adjusted Rand Index. *Comput. Stat.* 38, 327–347 (2023).
60. Karczewski, K. J. *et al.* The mutational constraint spectrum quantified from variation in 141,456 humans. *Nature* 581, 434–443 (2020).
61. Mikkola, M. *et al.* Lectin from Erythrina cristagalli Supports Undifferentiated Growth and Differentiation of Human Pluripotent Stem Cells. *https://home.liebertpub.com/scd* 22, 707–716 (2012).
62. Trokovic, R., Weltner, J. & Otonkoski, T. Generation of iPSC line HEL47.2 from healthy human adult fibroblasts. *Stem Cell Res.* 15, 263–265 (2015).

Main Tables

Name	Cell Type	Diagnosis	Sex	Derivation method	Characterized as iPSC	Marker expression	Ref	Registry info	Karyotype
HEL11.4	Skin fibroblast	Unaffected	Male	Retrovirus	Yes	Yes	[61]	Uhi007-B	46,X,inv(Y)(p11q11),add (1)(q12q21)
HEL47.2	Skin fibroblast	Unaffected	Male	Sendai virus	Yes	Yes	[62]	Uhi007-A	46,X,inv(Y)(p11q11)
HEL62.4	Skin fibroblast	Unaffected	Female	Sendai virus	Yes	Yes		Uhi020-A	47,XX,+12[2]/46,XX[18]
HEL61.1	Skin fibroblast	Unaffected	Female	Sendai virus	Yes	Yes		Uhi021-A	46, XX
HEL61.2	Skin fibroblast	Unaffected	Female	Sendai virus	Yes	Yes		Uhi021-B	46, XX
HEL82.6	Skin fibroblast	Unaffected	Female	Sendai virus	Yes	Yes		Uhi022-A	46, XX

Table 1. Cell lines used in the study with their corresponding donor information, derivation method, registration (https://hpscreg.eu/), and karyotype cytogenetic nomenclature.

Main Figures

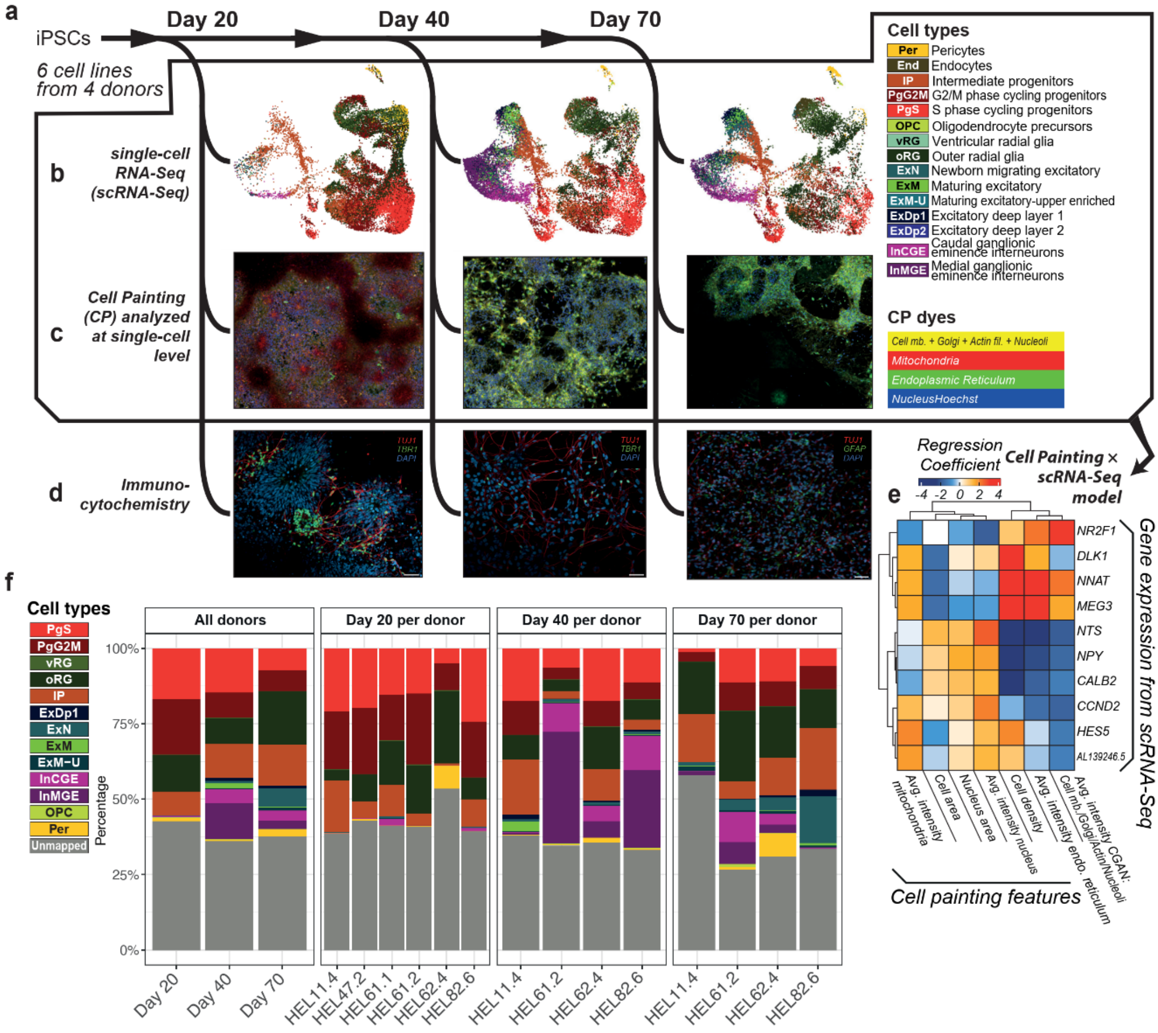

Figure 1. Overview of the experimental design and datasets. (a-d) Overview of the experiment. 6 iPSC lines from 4 donors were differentiated to cortical neural fate and assayed at days 20, 40 and 70 of the differentiation **(a)** using scRNA-seq **(b)**, Cell Painting (CP) **(c)** and immunocytochemistry (ICC) **(d)**. **(b)** UMAPs of cell types as identified by scRNA-seq analysis, split by time point. **(c-d)** Representative images from CP **(c)** and ICC **(d)** at each differentiation time point. Scale bar represents 50 µm. **(e)** Representative heatmap of the model linking expression of marker genes (rows) to CP image-based features (columns). **(f)** Cell type composition from the scRNA-seq dataset. The facet on the left represents aggregated cell type proportions across donors per time point, while the other facets represent individual timepoints, depicting cell type proportions for each donor. **Abbreviations:** PgS - S phase progenitors, PgG2M - G2M phase progenitors, vRG - ventral radial glia, oRG - outer radial glia, IP - intermediate progenitors, ExDp1/2 - Excitatory deep layer neurons 1/2, ExN - mirating excitatory neurons, ExM - maturing excitatory neurons, ExM-U - upper-layer enriched maturing excitatory neurons, InCGE - caudal ganglionic eminence interneurons, InMGE - medial ganglionic eminence interneurons, OPC - oligodendrocyte precursors, Per - pericytes, End - endothelial cells.

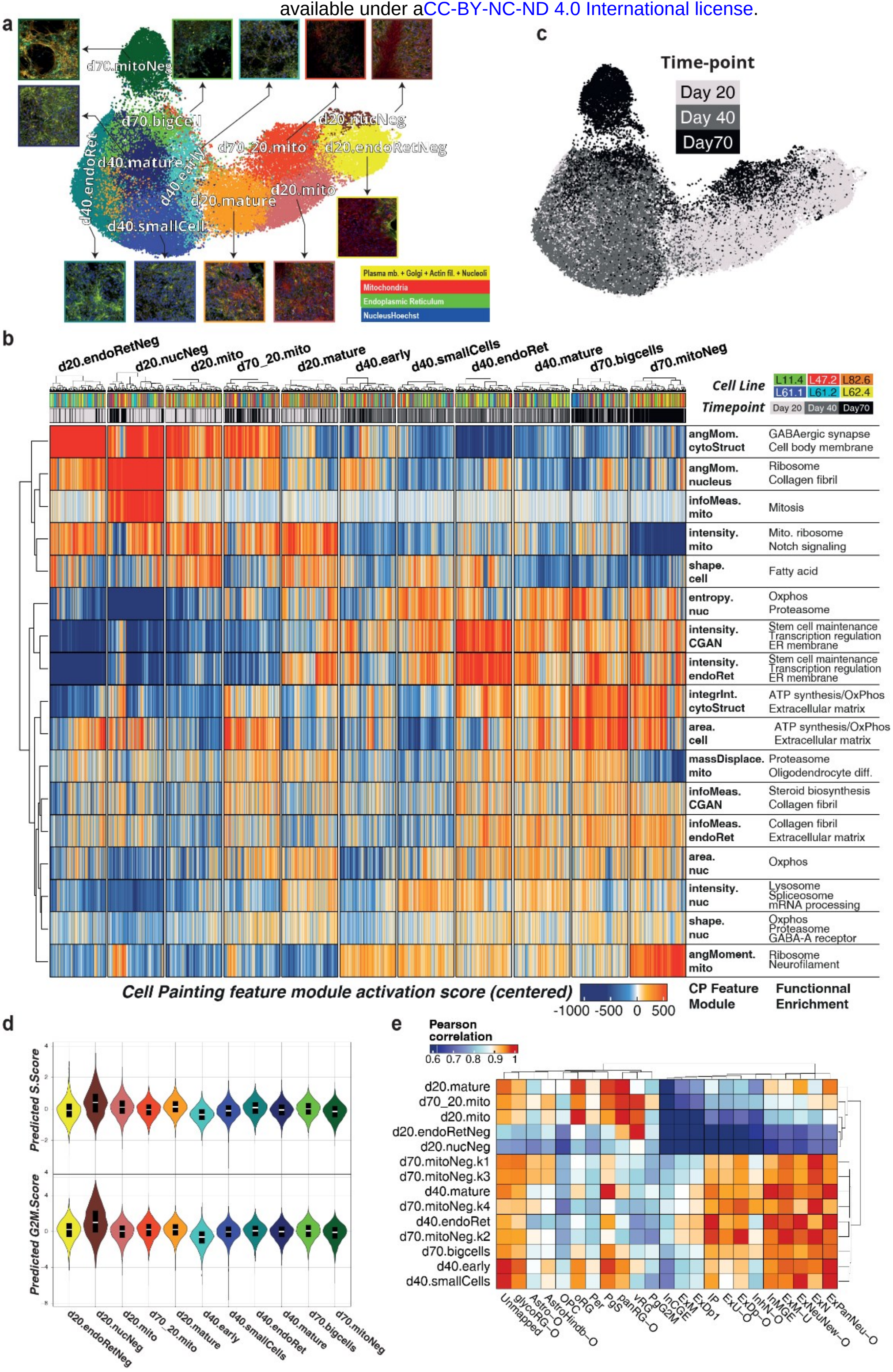

Figure 2. Cell Painting at the single-cell level. (a) UMAP of the Cell Painting dataset at the single-cell level. Cells are colored and labeled by Leiden clustering. A composite image representative of cells belonging to each CP cluster is indicated by arrows. **(b)** Heatmap of CP feature module activation score. 541 cells (minimum cluster size) were drawn from each CP cluster to ensure an equal contribution of each CP cluster to the Heatmap. The CP feature modules represent sets of CP features that are highly correlated. **(c)** Differentiation day (timepoints) projected on the CP UMAP. **(d)** Violin plots of predicted cell cycle scores per cell painting cluster. **(e)** Correlation heatmap of cell types to cell painting clusters, using marker CP features per CP cluster and predicted marker CP features per cell type as an anchor to compute the correlation.

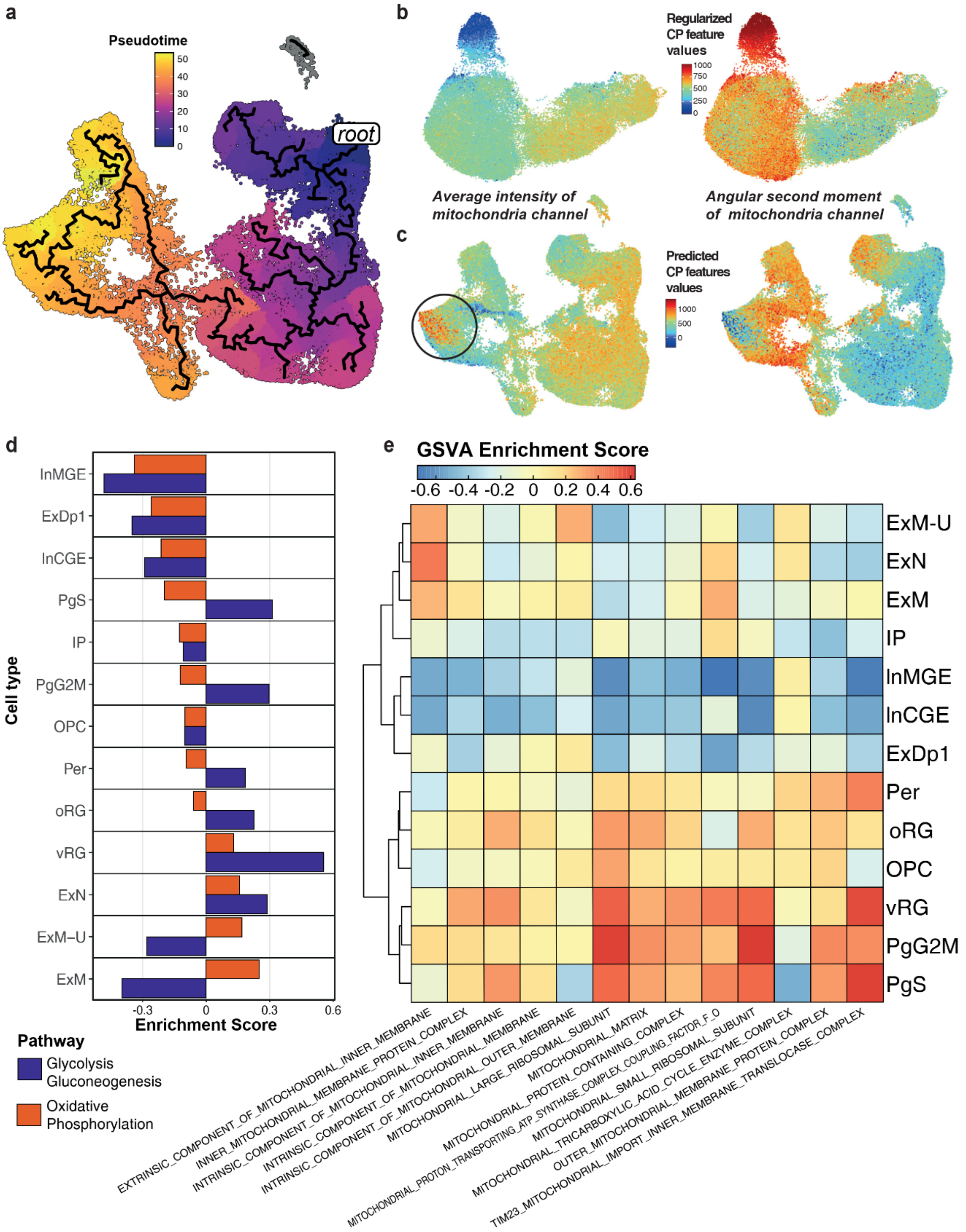

Figure 3. Mitochondrial feature dynamics in Cell Painting and gene expression. (a) Predicted pseudotime trajectory across timepoints in scRNA-seq showing progression from radial glia and progenitors, via intermediate progenitors, towards maturing excitatory and inhibitory neurons. Pseudotime is rooted in the predicted earliest node within day 20. **(b)** Feature values for mitochondrial intensity (left) and mitochondrial texture (right) projected onto the CP UMAP. **(c)** Predicted values for the CP features mitochondrial intensity (left) and texture (right) projected onto the scRNA-seq UMAP. **(d)** GSVA enrichment scores for glycolysis and oxidative phosphorylation pathways per pseudobulked cell type. Enrichment scores indicate a higher activation score of OxPhos in excitatory neurons, except for the deep layer 1 subtype (ExDp1). **(e)** GSVA enrichment scores for mitochondria-associated GO terms per pseudobulked cell type.

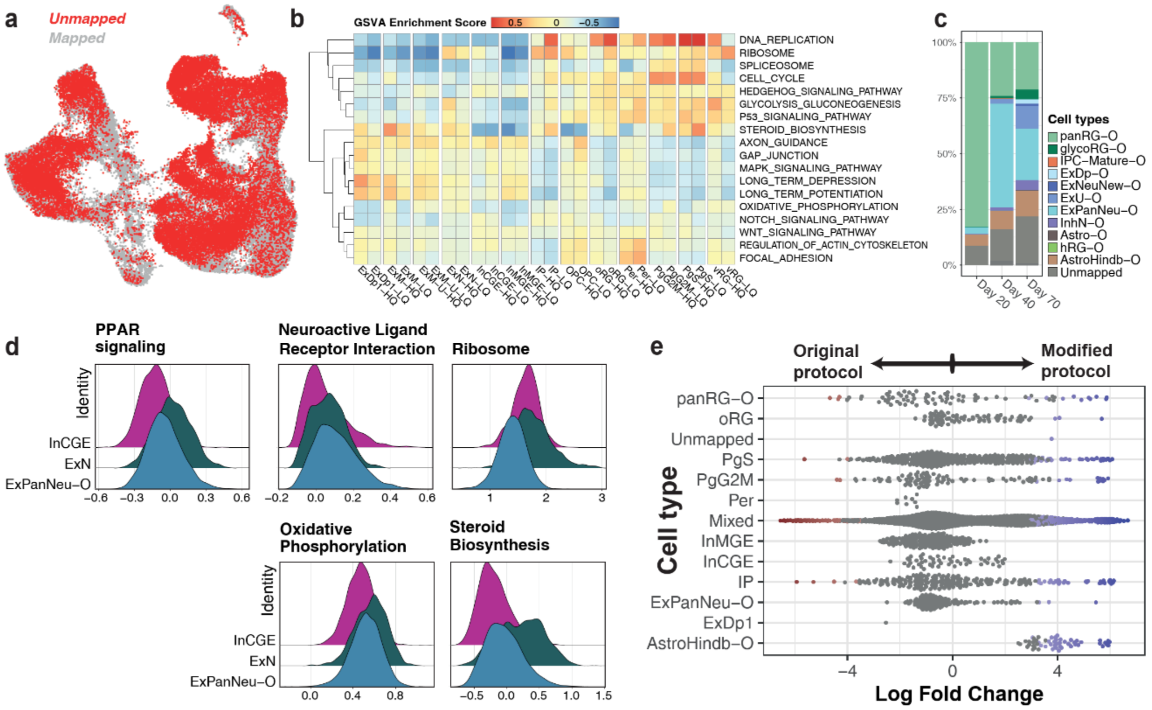

Figure 4. Characterization of low-quality cells within the scRNA-seq dataset. (a) UMAP of scRNA-seq data across timepoints with unmapped cells highlighted in red. **(b)** Enrichment scores from GSVA (across cell types) of key pathways driving the differences between high- and low-quality subsets per pseudobulked cell type. **(c)** Percentage of cells from the initial unmapped fraction that align to organoid cell types (Bhaduri *et al.*) per time point. **(d)** Ridge plots representing the distribution of module activation scores of key differentially activated pathways between pan-neuronal (ExPanNeu-O), excitatory (ExN) and inhibitory (InCGE) neuronal cell types. **(e)** Differential abundance of cell types produced by the original (left) or the modified (right) versions of the differentiation protocol, computed by MiloR. **Abbreviations:** panRG - pan radial glia, glycoRG - glycolytic radial glia, IPC-Mature - mature intermediate progenitors, ExDp - excitatory deep layer, ExNeuNew - newborn excitatory neurons, ExU - excitatory upper layer, ExPanNeu - pan-neuronal (excitatory), InhN - inhibitory neurons, Astro - astrocytes, hRG - hindbrain radial glia, AstroHindb - hindbrain astrocytes. “-O” differentiates organoid cell type annotations from the fetal.

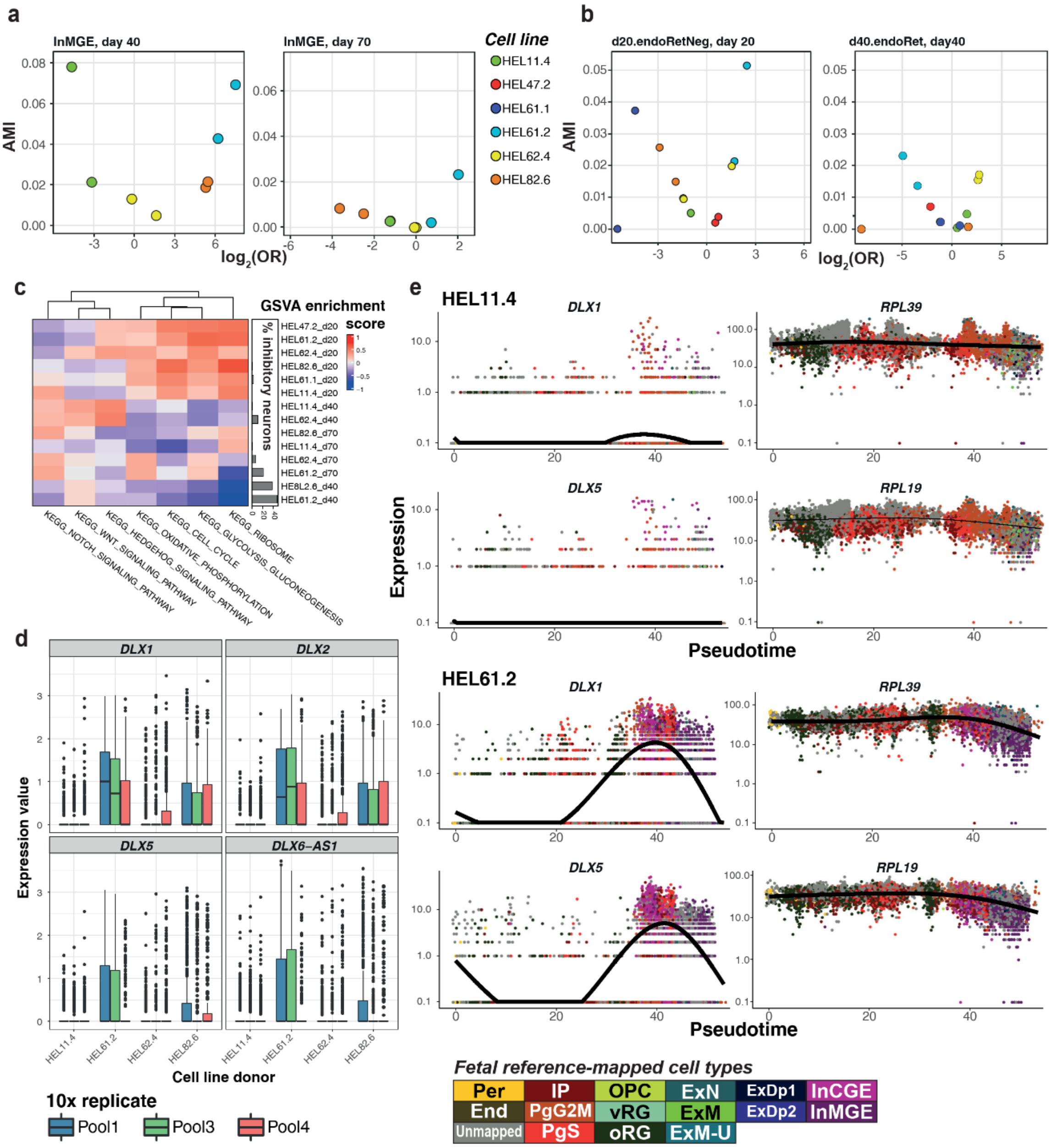

Figure 5. Mechanisms of donor-specific inhibitory neuron production. (a) AMI plots from scRNA-seq data within InMGE cells at days 40 and 70. Each point represents aggregate expression per technical replicate and donor. **(b)** AMI plots from CP data within the d20.endoRetNeg cluster at d20 and d40.endoRet at d40. Each point represents aggregate expression of all wells per induction replicate and donor. **(c)** GSVA enrichment scores from curated KEGG pathways between experimental populations (donor x timepoint) with hierarchical clustering on both axes. Annotation barplot to the right of the heatmap shows the percentage of cells produced by each experimental population annotated as inhibitory cell types (InCGE, InMGE, InhN-O). **(d)** Relative expression per donor (log-normalized values) of inhibitory interneuron-associated transcription factors within the progenitor pool (oRG+vRG+PgG2M+PgS) at day 40. The expression per donor is grouped per 10x sample. **(e)** Expression of interneuron-associated *DLX* genes and ribosomal subunits *RPL39* and *RPL19,* along pseudotime in two donors shown to produce a high (HEL61.2, left) and a low (HEL11.4, right) proportion of inhibitory neurons, respectively. Point colors represent fetal-annotated cell types.

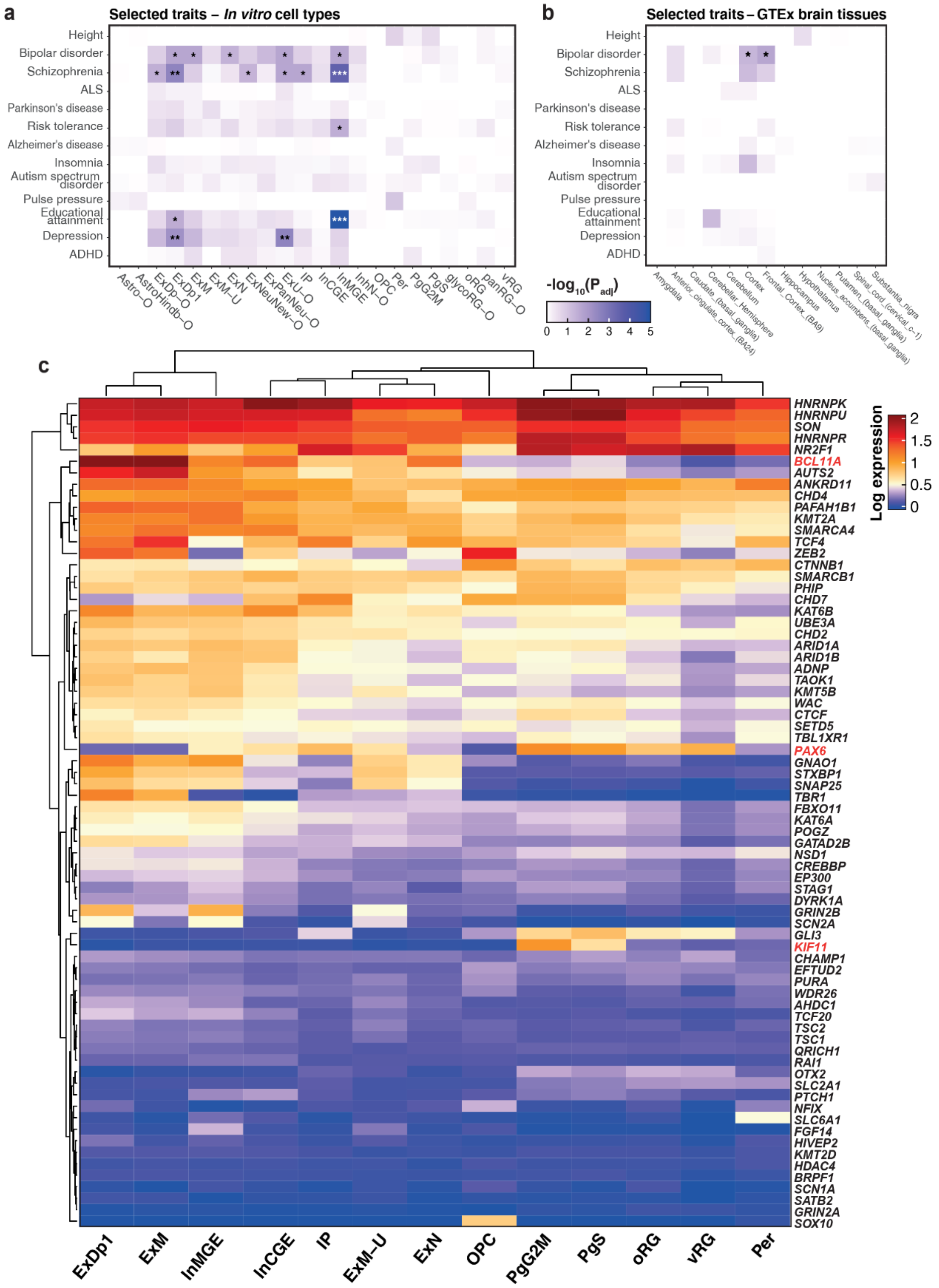

Figure 6. In vitro neurons capture brain-relevant traits. (a) Stratified LD score regression analysis shown for selected brain-related traits per cell type from our in vitro differentiation. Tile color represents the corresponding p values after multiple testing correction across traits and cell types, with the significance level indicated as follows: pAdj<0.05(*), pAdj<0.01(**) and pAdj<0.001 (***). **(b)** Stratified LD score regression analysis as in (a) per GTEx Brain tissue type. **(c)** Heatmap of normalized expression, pseudobulked per cell type, of brain-specific genes associated with developmental disorders (DDD study). Only DDD genes known to be highly intolerant to loss of function mutations are illustrated (n=72). Genes highlighted in red represent examples of cell type-specific expression.

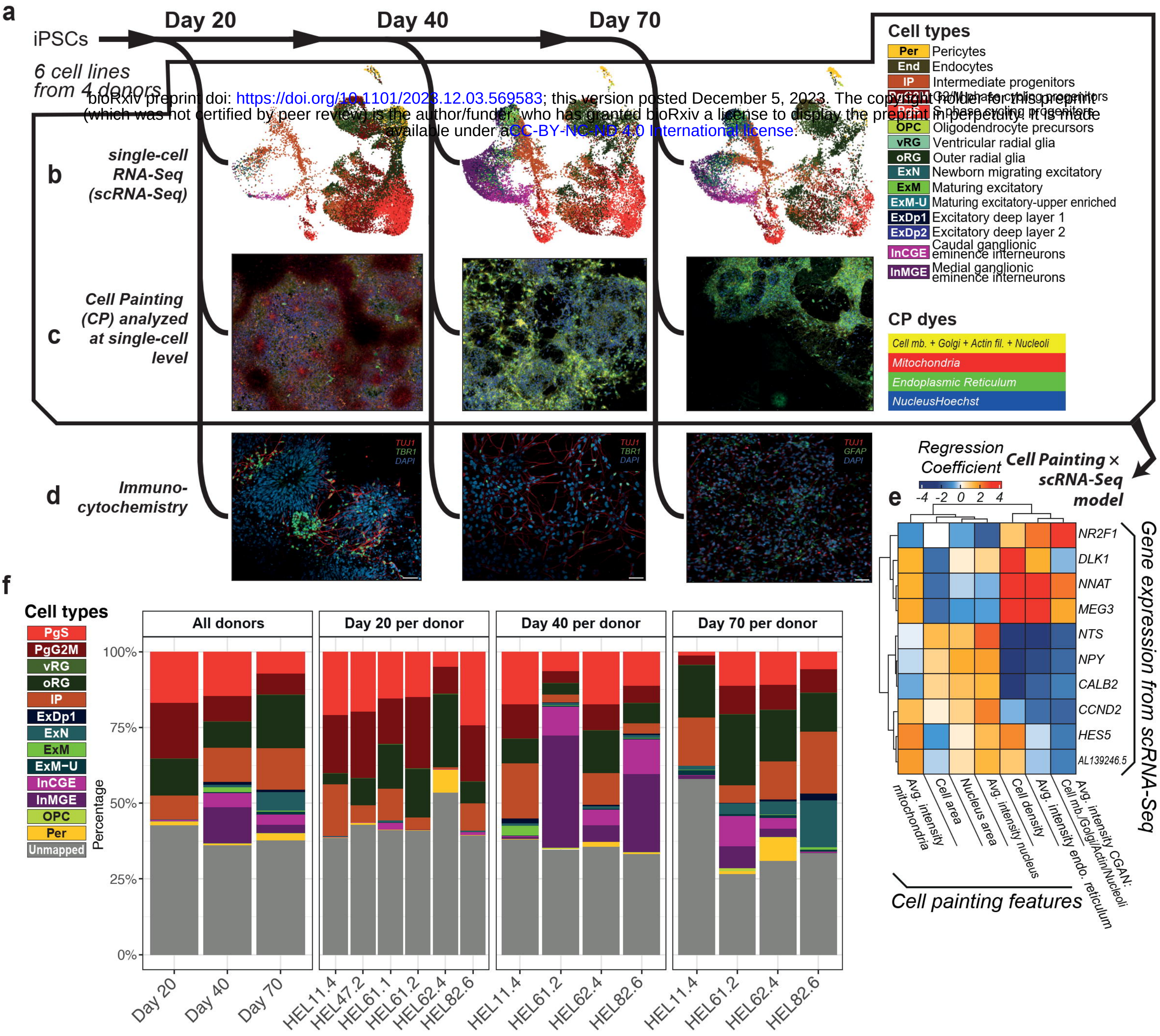
a
iPSCs
6 cell lines from 4 donors
Day 20
Day 40
Day 70
b
single-cell RNA-Seq (scRNA-Seq)
c
Cell Painting (CP) analyzed at single-cell level
d
Immuno-cytochemistry
TUJ1
TBR1
DAPI
TUJ1
TBR1
DAPI
TUJ1
GFAP
DAPI
Cell types
Per Pericytes
End Endocytes
IP Intermediate progenitors
PgG2M G2/M phase cycling progenitors
PgS S phase cycling progenitors
OPC Oligodendrocyte precursors
vRG Ventricular radial glia
oRG Outer radial glia
ExN Newborn migrating excitatory
ExM Maturing excitatory
ExM-U Maturing excitatory-upper enriched
ExDp1 Excitatory deep layer 1
ExDp2 Excitatory deep layer 2
InCGE Caudal ganglionic eminence interneurons
InMGE Medial ganglionic eminence interneurons
CP dyes
Cell mb. + Golgi + Actin fil. + Nucleoli
Mitochondria
Endoplasmic Reticulum
NucleusHoechst
Cell Painting × scRNA-Seq model
e
Regression Coefficient
-4 -2 0 2 4
NR2F1
DLK1
NNAT
MEG3
NTS
NPY
CALB2
CCND2
HES5
AL139246.5
Gene expression from scRNA-Seq
Avg. intensity mitochondria
Cell area
Nucleus area
Avg. intensity nucleus
Cell density
Avg. intensity endo. reticulum
Avg. intensity CGAN: Cell mb./Golgi/Actin/Nucleoli
Cell painting features
f
Cell types
PgS
PgG2M
vRG
oRG
IP
ExDp1
ExN
ExM
ExM−U
InCGE
InMGE
OPC
Per
Unmapped
Percentage
100%
75%
50%
25%
0%
All donors
Day 20 per donor
Day 40 per donor
Day 70 per donor
Day 20
Day 40
Day 70
HEL11.4
HEL47.2
HEL61.1
HEL61.2
HEL62.4
HEL82.6
HEL11.4
HEL61.2
HEL62.4
HEL82.6
HEL11.4
HEL61.2
HEL62.4
HEL82.6

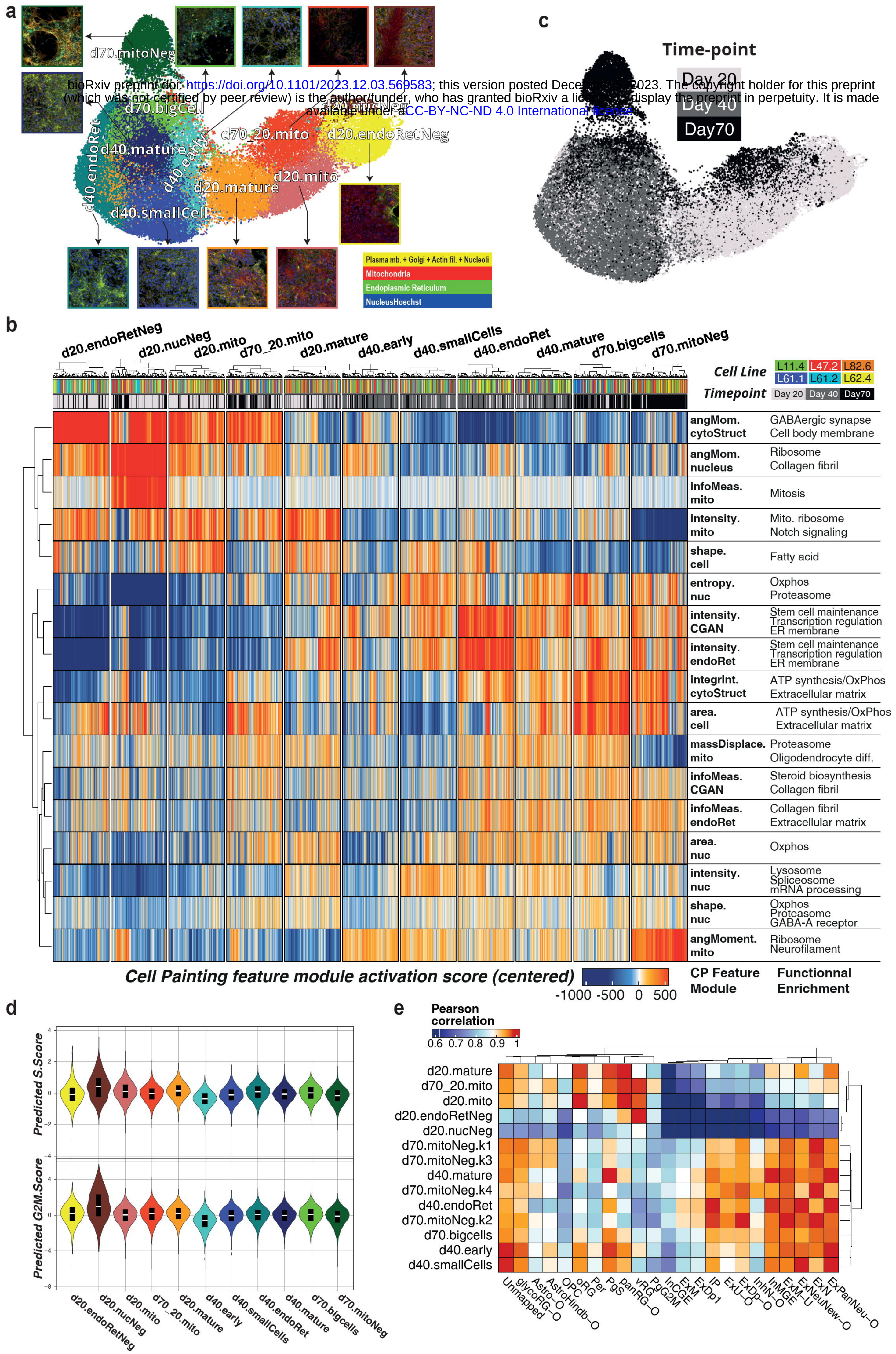
a
d70.mitoNeg
d70.bigCell
d70_20.mito
d20.endoRetNeg
d20.nucNeg
d40.endoRet
d40.mature
d40.early
d20.mature
d20.mito
d40.smallCell
Plasma mb. + Golgi + Actin fil. + Nucleoli
Mitochondria
Endoplasmic Reticulum
NucleusHoechst
c
Time-point
Day 20
Day 40
Day70
b
d20.endoRetNeg
d20.nucNeg
d20.mito
d70_20.mito
d20.mature
d40.early
d40.smallCells
d40.endoRet
d40.mature
d70.bigcells
d70.mitoNeg
Cell Line
L11.4
L47.2
L82.6
L61.1
L61.2
L62.4
Timepoint
Day 20
Day 40
Day70
angMom. cytoStruct
GABAergic synapse
Cell body membrane
angMom. nucleus
Ribosome
Collagen fibril
infoMeas. mito
Mitosis
intensity. mito
Mito. ribosome
Notch signaling
shape. cell
Fatty acid
entropy. nuc
Oxphos
Proteasome
intensity. CGAN
Stem cell maintenance
Transcription regulation
ER membrane
intensity. endoRet
Stem cell maintenance
Transcription regulation
ER membrane
integrInt. cytoStruct
ATP synthesis/OxPhos
Extracellular matrix
area. cell
ATP synthesis/OxPhos
Extracellular matrix
massDisplace. mito
Proteasome
Oligodendrocyte diff.
infoMeas. CGAN
Steroid biosynthesis
Collagen fibril
infoMeas. endoRet
Collagen fibril
Extracellular matrix
area. nuc
Oxphos
intensity. nuc
Lysosome
Spliceosome
mRNA processing
shape. nuc
Oxphos
Proteasome
GABA-A receptor
angMoment. mito
Ribosome
Neurofilament
Cell Painting feature module activation score (centered)
-1000 -500 0 500
CP Feature Module
Functionnal Enrichment
d
Predicted S.Score
Predicted G2M.Score
4
2
0
-2
-4
4
0
-4
-8
d20.endoRetNeg
d20.nucNeg
d20.mito
d70_20.mito
d20.mature
d40.early
d40.smallCells
d40.endoRet
d40.mature
d70.bigcells
d70.mitoNeg
e
Pearson correlation
0.6 0.7 0.8 0.9 1
d20.mature
d70_20.mito
d20.mito
d20.endoRetNeg
d20.nucNeg
d70.mitoNeg.k1
d70.mitoNeg.k3
d40.mature
d70.mitoNeg.k4
d40.endoRet
d70.mitoNeg.k2
d70.bigcells
d40.early
d40.smallCells
Unmapped
glycoRG–O
Astro–O
AstroHindb–O
OPC
oRG
Per
PgS
panRG–O
vRG
PgG2M
InCGE
ExM
ExDp1
IP
ExU–O
ExDp–O
InhN–O
InMGE
ExM–U
ExNeuNew–O
ExN
ExPanNeu–O

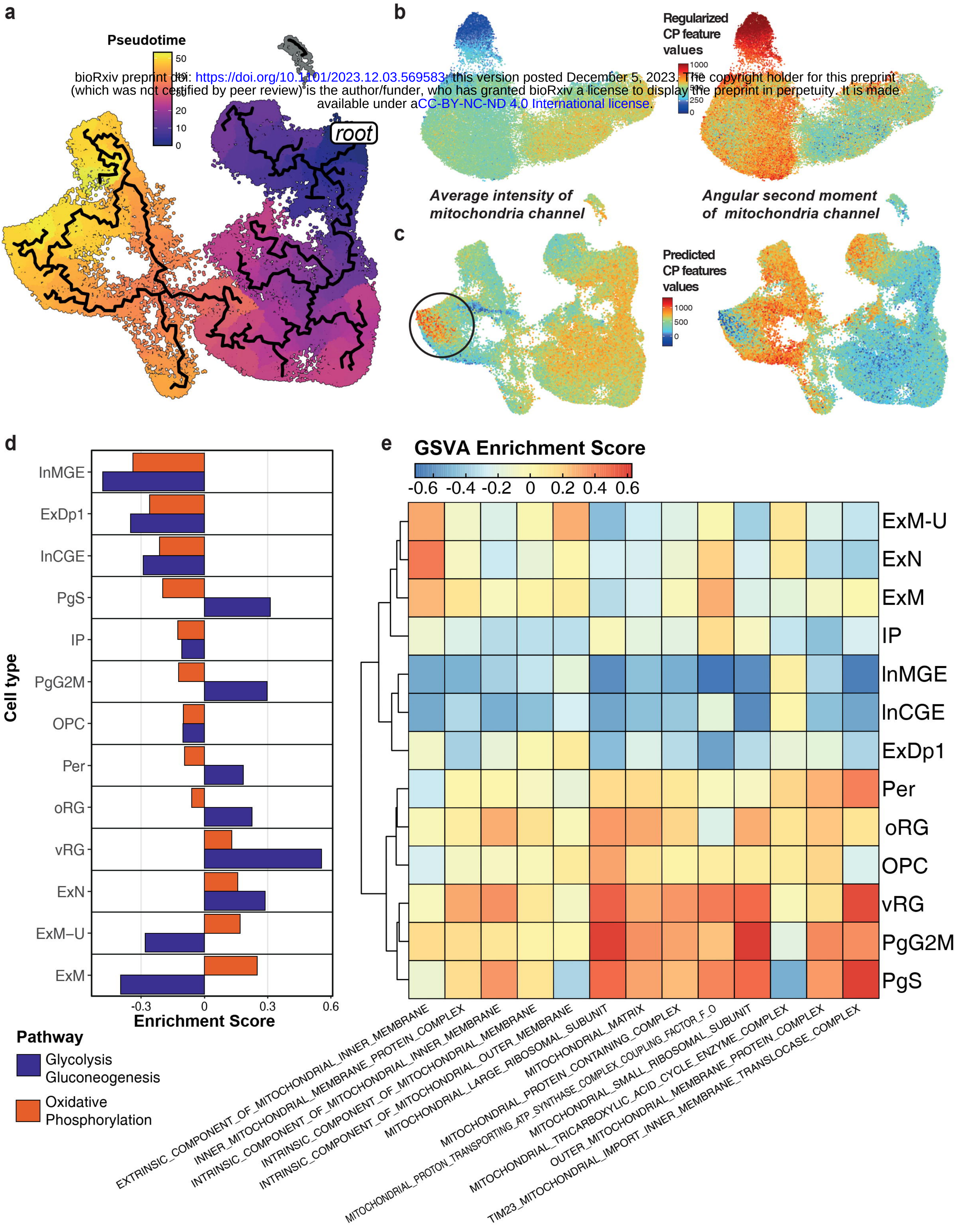
a
Pseudotime
50
40
30
20
10
0
root
b
Regularized
CP feature
values
1000
750
500
250
0
Average intensity of
mitochondria channel
Angular second moment
of mitochondria channel
c
Predicted
CP features
values
1000
500
0
d
InMGE
ExDp1
InCGE
PgS
IP
PgG2M
OPC
Per
oRG
vRG
ExN
ExM–U
ExM
Cell type
-0.3
0
0.3
0.6
Enrichment Score
Pathway
Glycolysis
Gluconeogenesis
Oxidative
Phosphorylation
e
GSVA Enrichment Score
-0.6
-0.4
-0.2
0
0.2
0.4
0.6
ExM-U
ExN
ExM
IP
InMGE
InCGE
ExDp1
Per
oRG
OPC
vRG
PgG2M
PgS
EXTRINSIC_COMPONENT_OF_MITOCHONDRIAL_INNER_MEMBRANE
INNER_MITOCHONDRIAL_MEMBRANE_PROTEIN_COMPLEX
INTRINSIC_COMPONENT_OF_MITOCHONDRIAL_INNER_MEMBRANE
INTRINSIC_COMPONENT_OF_MITOCHONDRIAL_MEMBRANE
INTRINSIC_COMPONENT_OF_MITOCHONDRIAL_OUTER_MEMBRANE
MITOCHONDRIAL_LARGE_RIBOSOMAL_SUBUNIT
MITOCHONDRIAL_MATRIX
MITOCHONDRIAL_PROTEIN_CONTAINING_COMPLEX
MITOCHONDRIAL_PROTON_TRANSPORTING_ATP_SYNTHASE_COMPLEX_COUPLING_FACTOR_F_O
MITOCHONDRIAL_SMALL_RIBOSOMAL_SUBUNIT
MITOCHONDRIAL_TRICARBOXYLIC_ACID_CYCLE_ENZYME_COMPLEX
OUTER_MITOCHONDRIAL_MEMBRANE_PROTEIN_COMPLEX
TIM23_MITOCHONDRIAL_IMPORT_INNER_MEMBRANE_TRANSLOCASE_COMPLEX

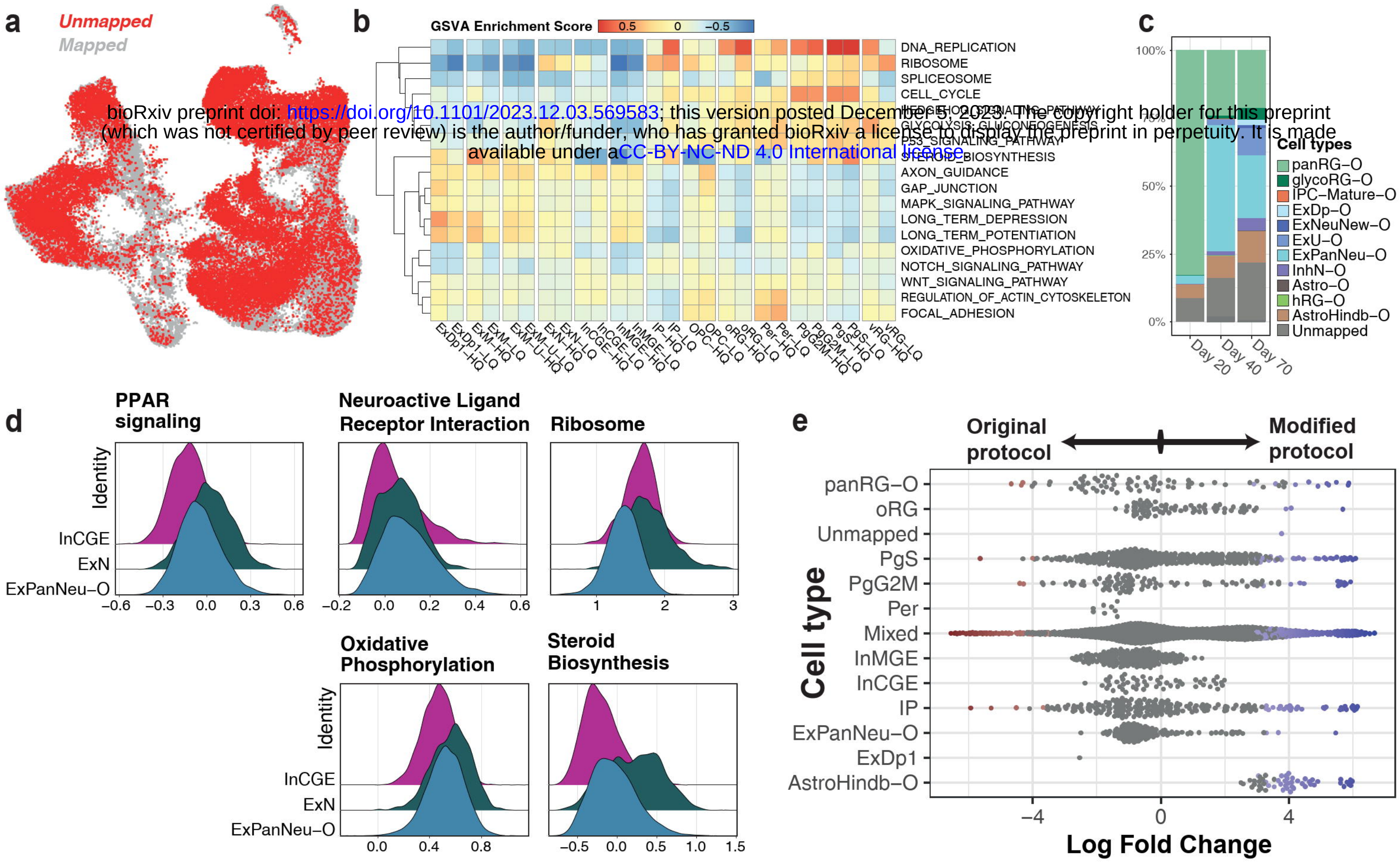
a
Unmapped
Mapped
b
GSVA Enrichment Score
0.5
0
−0.5
DNA_REPLICATION
RIBOSOME
SPLICEOSOME
CELL_CYCLE
HEDGEHOG_SIGNALING_PATHWAY
GLYCOLYSIS_GLUCONEOGENESIS
P53_SIGNALING_PATHWAY
STEROID_BIOSYNTHESIS
AXON_GUIDANCE
GAP_JUNCTION
MAPK_SIGNALING_PATHWAY
LONG_TERM_DEPRESSION
LONG_TERM_POTENTIATION
OXIDATIVE_PHOSPHORYLATION
NOTCH_SIGNALING_PATHWAY
WNT_SIGNALING_PATHWAY
REGULATION_OF_ACTIN_CYTOSKELETON
FOCAL_ADHESION
ExDp1−HQ
ExDp1−LQ
ExM−HQ
ExM−LQ
ExM−U−HQ
ExM−U−LQ
ExN−HQ
ExN−LQ
InCGE−HQ
InCGE−LQ
InMGE−HQ
InMGE−LQ
IP−HQ
IP−LQ
OPC−HQ
OPC−LQ
oRG−HQ
oRG−LQ
Per−HQ
Per−LQ
PgG2M−HQ
PgG2M−LQ
PgS−HQ
PgS−LQ
vRG−HQ
vRG−LQ
c
100%
75%
50%
25%
0%
Day 20
Day 40
Day 70
Cell types
panRG−O
glycoRG−O
IPC−Mature−O
ExDp−O
ExNeuNew−O
ExU−O
ExPanNeu−O
InhN−O
Astro−O
hRG−O
AstroHindb−O
Unmapped
d
PPAR signaling
Neuroactive Ligand Receptor Interaction
Ribosome
Identity
InCGE
ExN
ExPanNeu−O
−0.6
−0.3
0.0
0.3
0.6
−0.2
0.0
0.2
0.4
0.6
1
2
3
Oxidative Phosphorylation
Steroid Biosynthesis
Identity
InCGE
ExN
ExPanNeu−O
0.0
0.4
0.8
−0.5
0.0
0.5
1.0
1.5
e
Original protocol
Modified protocol
Cell type
panRG−O
oRG
Unmapped
PgS
PgG2M
Per
Mixed
InMGE
InCGE
IP
ExPanNeu−O
ExDp1
AstroHindb−O
−4
0
4
Log Fold Change

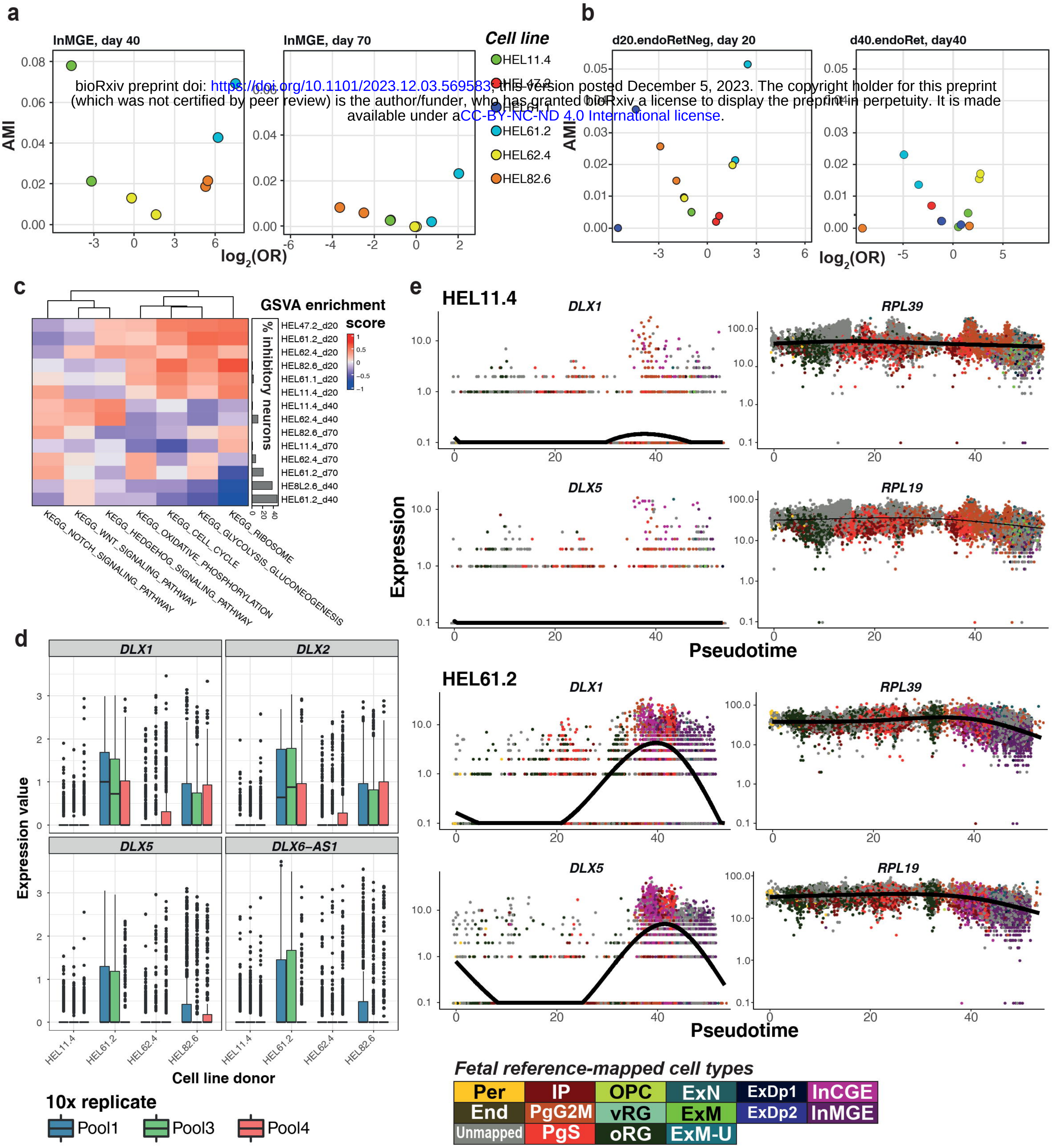
a
InMGE, day 40
InMGE, day 70
AMI
log2(OR)
0.08
0.06
0.04
0.02
0.00
-3
0
3
6
-6
-4
-2
2
Cell line
HEL11.4
HEL47.2
HEL61.1
HEL61.2
HEL62.4
HEL82.6
b
d20.endoRetNeg, day 20
d40.endoRet, day40
0.05
0.04
0.03
0.02
0.01
-5
5
c
GSVA enrichment score
% inhibitory neurons
1
0.5
0
−0.5
−1
HEL47.2_d20
HEL61.2_d20
HEL62.4_d20
HEL82.6_d20
HEL61.1_d20
HEL11.4_d20
HEL11.4_d40
HEL62.4_d40
HEL82.6_d70
HEL11.4_d70
HEL62.4_d70
HEL61.2_d70
HE8L2.6_d40
HEL61.2_d40
0
20
40
KEGG_NOTCH_SIGNALING_PATHWAY
KEGG_WNT_SIGNALING_PATHWAY
KEGG_HEDGEHOG_SIGNALING_PATHWAY
KEGG_OXIDATIVE_PHOSPHORYLATION
KEGG_CELL_CYCLE
KEGG_GLYCOLYSIS_GLUCONEOGENESIS
KEGG_RIBOSOME
d
DLX1
DLX2
DLX5
DLX6−AS1
Expression value
Cell line donor
HEL11.4
HEL61.2
HEL62.4
HEL82.6
10x replicate
Pool1
Pool3
Pool4
e
HEL11.4
HEL61.2
DLX1
DLX5
RPL39
RPL19
Expression
Pseudotime
100.0
10.0
1.0
0.1
Fetal reference-mapped cell types
Per
IP
OPC
ExN
ExDp1
InCGE
End
PgG2M
vRG
ExM
ExDp2
InMGE
Unmapped
PgS
oRG
ExM-U

Figure 5

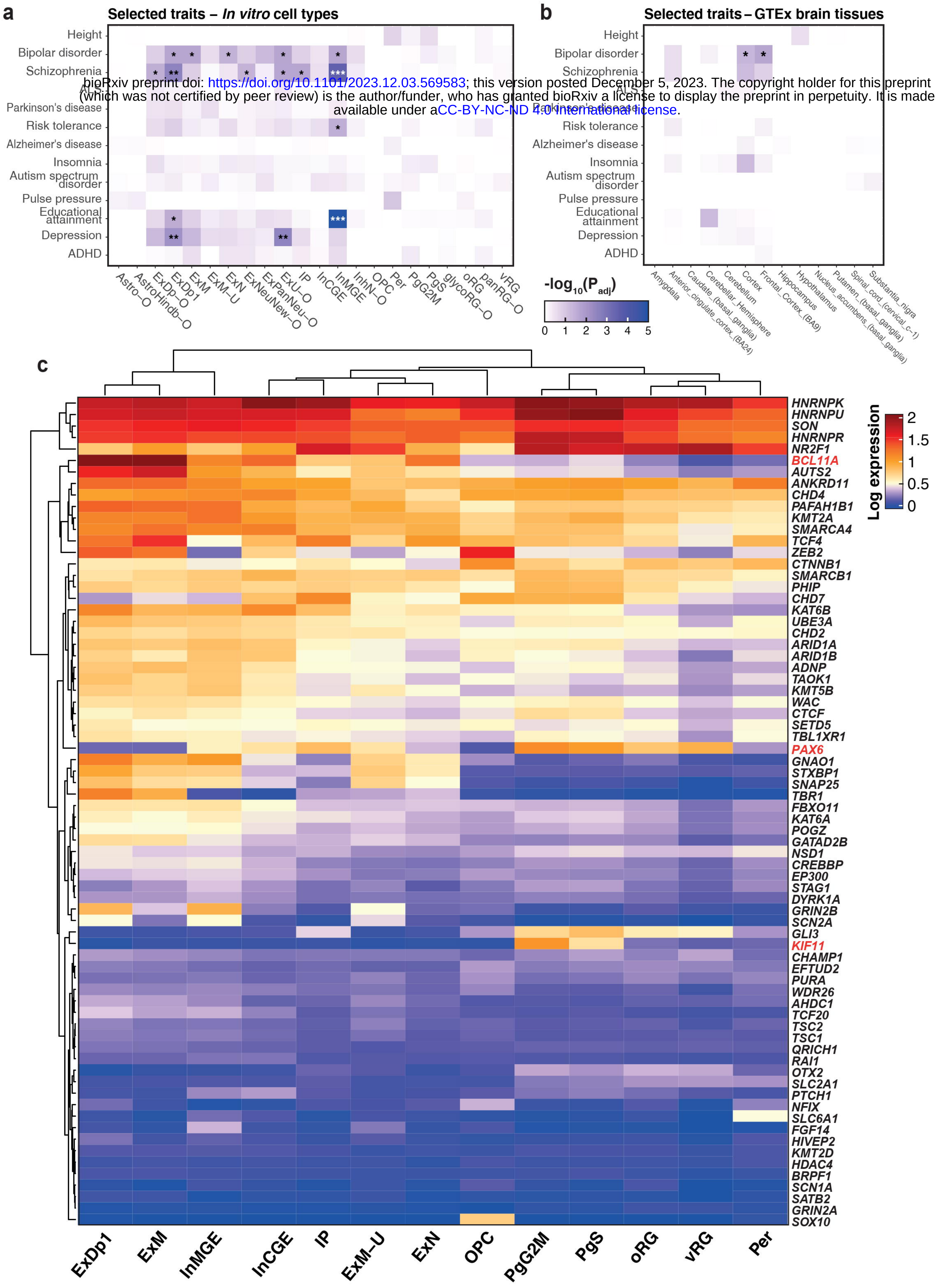
a
Selected traits – In vitro cell types
Height
Bipolar disorder
Schizophrenia
ALS
Parkinson's disease
Risk tolerance
Alzheimer's disease
Insomnia
Autism spectrum disorder
Pulse pressure
Educational attainment
Depression
ADHD
Astro–O
AstroHindb–O
ExDp–O
ExDp1
ExM
ExM–U
ExN
ExNeuNew–O
ExPanNeu–O
ExU–O
IP
InCGE
InMGE
InhN–O
OPC
Per
PgG2M
PgS
glycoRG–O
oRG
panRG–O
vRG
*
**
***
b
Selected traits – GTEx brain tissues
Height
Bipolar disorder
Schizophrenia
ALS
Parkinson's disease
Risk tolerance
Alzheimer's disease
Insomnia
Autism spectrum disorder
Pulse pressure
Educational attainment
Depression
ADHD
Amygdala
Anterior_cingulate_cortex_(BA24)
Caudate_(basal_ganglia)
Cerebellar_Hemisphere
Cerebellum
Cortex
Frontal_Cortex_(BA9)
Hippocampus
Hypothalamus
Nucleus_accumbens_(basal_ganglia)
Putamen_(basal_ganglia)
Spinal_cord_(cervical_c-1)
Substantia_nigra
-log$_{10}$(P$_{adj}$)
0
1
2
3
4
5
c
HNRNPK
HNRNPU
SON
HNRNPR
NR2F1
BCL11A
AUTS2
ANKRD11
CHD4
PAFAH1B1
KMT2A
SMARCA4
TCF4
ZEB2
CTNNB1
SMARCB1
PHIP
CHD7
KAT6B
UBE3A
CHD2
ARID1A
ARID1B
ADNP
TAOK1
KMT5B
WAC
CTCF
SETD5
TBL1XR1
PAX6
GNAO1
STXBP1
SNAP25
TBR1
FBXO11
KAT6A
POGZ
GATAD2B
NSD1
CREBBP
EP300
STAG1
DYRK1A
GRIN2B
SCN2A
GLI3
KIF11
CHAMP1
EFTUD2
PURA
WDR26
AHDC1
TCF20
TSC2
TSC1
QRICH1
RAI1
OTX2
SLC2A1
PTCH1
NFIX
SLC6A1
FGF14
HIVEP2
KMT2D
HDAC4
BRPF1
SCN1A
SATB2
GRIN2A
SOX10
Log expression
2
1.5
1
0.5
0
ExDp1
ExM
InMGE
InCGE
IP
ExM–U
ExN
OPC
PgG2M
PgS
oRG
vRG
Per